Interaction dependence of the Hall response for the Bose-Hubbard triangular ladder

Catalin-Mihai Halati and Thierry Giamarchi
Department of Quantum Matter Physics, University of Geneva, Quai Ernest-Ansermet 24, 1211 Geneva, Switzerland

(Received 23 September 2024; accepted 11 March 2025; published 2 May 2025)

We explore the behavior of the Hall response of a Bose-Hubbard triangular ladder in a magnetic field as a function of the repulsive on-site atomic interactions. We consider a wide range of interaction strengths, from the weakly interacting limit to the hard-core regime. This is realized by computing the Hall polarization following the quench of a weak linear potential, which induces the flow of a current through the system, using time-dependent matrix product state numerical simulations. We complement our understanding in the regime of small magnetic fields by analytical calculations of the equilibrium value of the Hall polarization for noninteracting bosonic atoms and under a mean-field assumption. The Bose-Hubbard triangular flux ladder exhibits a rich phase diagram, containing Meissner, vortex, and biased-chiral, superfluid phases. We show that the Hall response can be employed to fingerprint the various chiral states, the frustration effects occurring in the limit of strong interactions, and the phase boundaries of the equilibrium phase diagram.

DOI: 10.1103/PhysRevResearch.7.023112

I. INTRODUCTION

Strongly correlated topological matter exhibits exotic properties like particles with fractional quantum numbers and anyonic exchange statistics, which offer a promising avenue for quantum computing applications [1,2]. One of the paradigmatic examples of topological quantum states is the fractional quantum Hall state [3–5], stemming from the interplay of strong interactions and magnetic fields. The realization of such topologically nontrivial states has been an important goal for ultracold atom platforms. As in these systems the atoms are neutral the magnetic fields are artificially realized, e.g., by coupling to laser light via Raman processes [6–8]. This technique has led to the experimental realization of artificial magnetic fields for atoms confined to quasi-one-dimensional ladders, or two-dimensional geometries, for both bosonic and fermionic atomic species [9–19]. Furthermore, recently a Laughlin-type fractional quantum Hall state of two atoms has been prepared [20].

One of the central questions in the field is related to the design of experimentally relevant probes that can unravel the nontrivial topological properties of the prepared quantum states. In solid-state materials, the Hall effect, i.e., monitoring the induced transverse current upon the application of a force, has been a widely employed transport measurement. More recently, the Hall response has become accessible for ultracold atoms in optical lattices, and for weakly interacting gases, has been measured from the center-of-mass drifts or local currents [14,17,18]. Furthermore, theoretical proposals relate the quantized Hall response to topological invariants for small interacting ensembles for identifying the fractional states [21,22]. However, a complete understanding of the behavior of the Hall response when strong interactions are present is still lacking. Theoretical progress is being made in the case of ladder systems [23–28], the minimal setups for the study of the interplay of interactions and orbital effects, or by making use of special geometries [29–32]. In particular, the theoretical prediction of a universal Hall response occurring for certain parameters for interacting fermionic ladders [25] has been experimentally confirmed [19]. For ladders, a universal relation between the Hall resistance and the charge stiffness has also been proposed [27].

In this paper, we explore the Hall response for a Bose-Hubbard triangular ladder under the action of a magnetic field, focusing on the behavior of the Hall polarization for a wide range of on-site atomic interactions. This is motivated by recent studies, which showed that the Hall response can be employed as a sensitive probe for the features of the underlying phase diagram, either in the case of hard-core bosons in the triangular geometry [28], or in the limit of small magnetic fields for square ladders [27]. Furthermore, triangular flux ladders have proven to exhibit rich phase diagrams [33–45], with frustration-induced effects and phases without an equivalent in the unfrustrated square geometry [41].

The plan of the paper is as follows: In Sec. II, we describe the model we investigate and the protocol employed for the numerical calculation of the Hall polarization. We then briefly present the main message of our results in Sec. III. In Sec. IV, we briefly present the numerical method based on matrix product states employed in this paper, while in Sec. V, we perform analytical calculations in the noninteracting and mean-field limits for computing the equilibrium Hall polarization. The results are presented in Sec. VI, focusing first on the behavior in the Meissner superfluid phase (Sec. VI B), followed by an analysis around the phase transition boundaries (Sec. VI C), in the biased-chiral superfluid phase (Sec. VI D),

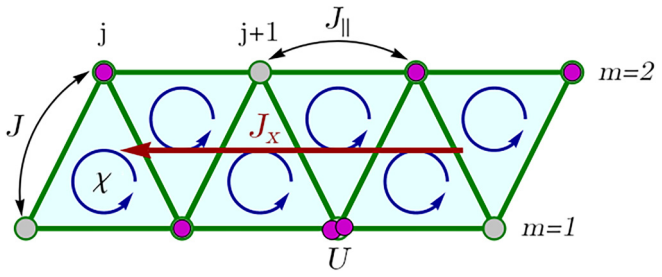

FIG. 1. Sketch of the triangular flux ladder model. The legs are denoted by $m = 1, 2$, and the sites on each leg are numbered by j. The bosonic atoms can tunnel along the rungs with amplitude J and along the legs with amplitude $J_\parallel$. We take into account repulsive on-site interactions between the atoms of strength U, and a flux χ pierces each triangular plaquette. Because of the presence of a linear potential V_x, a current $\boldsymbol{J}_x$ passes through the ladder.

followed by a discussion of the commensurability effects occurring in the vortex superfluid phase (Sec. VI E). We discuss our results and conclude in Sec. VII.

II. MODEL AND PROTOCOL

We consider interacting bosonic atoms confined to a triangular ladder under the action of a magnetic field, as sketched in Fig. 1. The Hamiltonian of the Bose-Hubbard model in a magnetic field is given by [41]

$$\begin{aligned} H &= H_\parallel + H_\perp + H_{\rm int}, \\ H_\parallel &= -J_\parallel \sum_{j=1}^{L-1} (e^{-i\chi} b^\dagger_{j,1} b_{j+1,1} + \text{H.c.}) \\ &\quad - J_\parallel \sum_{j=1}^{L-1} (e^{i\chi} b^\dagger_{j,2} b_{j+1,2} + \text{H.c.}), \\ H_\perp &= -J \sum_{j=1}^{L} (b^\dagger_{j,1} b_{j,2} + \text{H.c.}) \\ &\quad - J \sum_{j=1}^{L-1} (b^\dagger_{j+1,1} b_{j,2} + \text{H.c.}), \\ H_{\rm int} &= \frac{U}{2} \sum_{j=1}^{L} \sum_{m=1}^{2} n_{j,m}(n_{j,m} - 1). \end{aligned} \tag{1}$$

We denote by $b_{j,m}$ and $b^\dagger_{j,m}$ the bosonic annihilation and creation operators at position j and leg $m = 1, 2$. $\rho = N/(2L)$ represents the atomic filling, with the total number of particles $N = \sum_{j=1}^{L} \sum_{m=1}^{2} n_{j,m}$ and L the number of sites on each leg of the ladder. $H_\parallel$ gives the tunneling along the two legs of the ladder, with amplitude $J_\parallel$. The complex value of the tunneling amplitude stems from the presence of a magnetic field, with strength characterized by the flux χ [6,7]. The tunneling along the rungs of the ladder is described by $H_\perp$ with amplitude J. The atoms interact repulsively if on the same lattice site, with the interaction strength $U > 0$. We assume $\hbar = 1$ in the following. This model has a rich phase diagram of chiral quantum phases, as discussed in Refs. [28,41]. We give an overview of the phase diagrams for the considered parameter regimes in Sec. VI.

We are interested in the Hall response of the system and its dependence on the on-site interaction strength for the different phases present. To realize this, we monitor the dynamics of the system following the quench of a linear potential in the x direction,

$$V_x = \mu \sum_{j=1}^{L} \sum_{m=1}^{2} \left[j + \frac{1}{2}(m-1) \right] n_{j,m}. \tag{2}$$

This protocol has been investigated for square ladders in Refs. [25,26], and was analyzed for the triangular ladder in the limit of hard-core interactions in Ref. [28]. Furthermore, it has been experimentally implemented for interacting fermionic atoms on a square ladder in Ref. [19]. In order to compute the Hall response, we begin with the system in its ground state at time $tJ = 0$. Following the quench with the potential V_x at $t > 0$ a total current $\boldsymbol{J}_x$ is present in the x direction and, because of the presence of the magnetic flux, between the two legs of the ladder a density imbalance P_y develops. These observables are defined for the triangular ladder as

$$\begin{aligned} P_y &= \sum_j (n_{j,1} - n_{j,2}), \\ \boldsymbol{J}_x &= -i \sum_j \Big[\frac{J}{2} (b^\dagger_{j,1} b_{j,2} + b^\dagger_{j,2} b_{j+1,1} - \text{H.c.}) \\ &\quad + J_\parallel (e^{-i\chi} b^\dagger_{j,1} b_{j+1,1} + e^{i\chi} b^\dagger_{j,2} b_{j+1,2} - \text{H.c.}) \Big], \end{aligned} \tag{3}$$

where in the current J_x we have contributions from the two legs of the ladder and also from the rungs owing to the triangular geometry. For its derivation see Refs. [28,46]. A current flowing towards smaller values of the index j corresponds to negative values of $\boldsymbol{J}_x$.

The Hall response of the system is quantified by the Hall polarization, defined as the ratio of the two observables defined in Eq. (3) [25,26]

$$P_H(t) = \frac{\langle P_y \rangle(t)}{\langle \boldsymbol{J}_x \rangle(t)/J}. \tag{4}$$

In the numerator, we usually consider the imbalance difference with respect to the ground-state value, $\langle P_y \rangle(t) - \langle P_y \rangle(0)$, as phases like the biased-chiral superfluid exhibit a finite value of the imbalance in equilibrium.

The usefulness of employing the Hall polarization as a measure of the response stems from the fact that even though the magnitudes of the density imbalance and total current grow under the action of the linear potential $P_H(t)$ stabilizes to a transient steady value at intermediate times [25,26,28]. We compute $P_H(t)$ numerically using time-dependent matrix product states methods as described in Sec. IV and its equilibrium value analytically in the noninteracting or mean-field limits in Sec. V. The steady value of the Hall polarization we denote by $\langle\langle P_H \rangle\rangle$, where we performed the average over $P_H(t)$ for a time interval of at least $10/J$. We work in a regime of small values of the linear potential μ/J, such that the results shown are independent of its value. However, if we decrease the value of the potential, we have access to longer times in

the dynamics before the finite-size effects become relevant. We note that we have discussed the influence of μ/J in more detail for the hard-core case in Ref. [28].

III. KEY RESULTS

Our paper aims to understanding the behavior of the Hall response of the quantum chiral phases occurring for interacting bosonic particles on a triangular ladder geometry. We show that the Hall polarization, computed numerically following the quench of a linear potential, is a reliable observable of quantifying the Hall response for the triangular ladder for all strengths of interactions considered. We focus our discussion on the most striking features observed in the Hall polarization, how they correlate with the underlying ground-state phase diagram, and the behavior obtained by varying the local interactions.

We show that the Hall response is extremely sensitive to the phase boundaries, in particular, as we approach the transition thresholds within the Meissner superfluid phase, where a divergent-like behavior is observed. By comparing the numerical results with analytical expressions obtained in the noninteracting limit, we attribute the divergence to the expected vanishing of the current at the phase transition owing to changes in the structure of the lower energy band. While one might expect a large negative Hall response even if weak interactions are added, interestingly, we obtain large values close to the transition threshold also in the strongly correlated regimes.

We find several instances in which the Hall polarization changes sign. In the Meissner phase, the sign can be changed by varying the interaction strength for certain values of the atomic filling, stemming from the presence of particle-hole symmetry in the hard-core limit for half filling. In the vortex phase, the sign of the Hall response may depend on both the hopping amplitudes and the magnetic flux.

The presence of frustration induced vortex commensurability effects in the vortex phase determines a large positive Hall polarization. Previously, we discussed that in the hard-core case, having a second commensurate vortex density in the current pattern of the vortex state is correlated with a strong Hall response [28]. Here, we extend these results by showing that the competition between incommensurate and commensurate vortices is present even for finite, but large, values of the on-site interactions, and that the Hall polarization is sensitive to these nontrivial effects.

IV. MATRIX PRODUCT STATES NUMERICAL METHODS

In the following, we briefly describe the numerical approaches used in this paper. To numerically obtain the ground state of the Hamiltonian H, Eq. (1), we employed a finite-size density matrix renormalization group (DMRG) algorithm in the matrix product state (MPS) representation [47–51], implemented using the ITensor library [52]. We consider ladders with a number of sites on each leg of $L = 60$ and $L = 90$, and with a maximal bond dimension up to 500, ensuring that the truncation error is at most 10^{-10}. Since we are considering a bosonic model with finite interactions, the local Hilbert space is large, thus a cutoff for its dimension is needed. We use a maximal local dimension of at least four or five states per site, depending on the value of the interactions.

The time evolution with the additional potential $H + V_x$, Eq. (2), is performed using the time-dependent matrix product state method (tMPS) based on the Trotter-Suzuki decomposition [49,53,54]. The convergence was ensured with a time step of $\mathrm{d}tJ/\hbar = 0.01$ and the measurements were performed every tenth time step. We maintain the same bond dimension as for the ground-state search, which ensures that, up to the times considered in this paper, the truncation error is at most 10^{-9}.

V. ANALYTICAL CALCULATION OF THE EQUILIBRIUM HALL POLARIZATION

In Refs. [25,26] it was shown that the transient steady value $\langle\langle P_H\rangle\rangle$ agrees with the equilibrium Hall polarization obtained for periodic boundary conditions upon the threading of a flux through the system. In the following, we derive the equilibrium value analytically for the noninteracting case for small values of the flux χ and using a mean-field approach in the Meissner phase.

The Hamiltonian of the system for periodic boundary conditions in the x direction, upon the threading of a flux $\tilde{\Phi}$ through the cylinder and under the action of a potential difference between the two legs of the ladder is given by

$$\begin{aligned}\tilde{H} = & -J_{\parallel}\sum_{j=1}^{L}(e^{-i\chi-i\tilde{\Phi}/L}b^{\dagger}_{j,1}b_{j+1,1}+\text{H.c.})\\ & -J_{\parallel}\sum_{j=1}^{L}(e^{i\chi-i\tilde{\Phi}/L}b^{\dagger}_{j,2}b_{j+1,2}+\text{H.c.})\\ & -J\sum_{j=1}^{L}(e^{-i\tilde{\Phi}/2L}b^{\dagger}_{j,1}b_{j,2}+e^{i\tilde{\Phi}/2L}b^{\dagger}_{j+1,1}b_{j,2}+\text{H.c.})\\ & +\frac{U}{2}\sum_{j=1}^{L}\sum_{m=1}^{2}n_{j,m}(n_{j,m}-1)\\ & +E_y\sum_{j=1}^{L}(n_{j,1}-n_{j,2}),\end{aligned} \tag{5}$$

where E_y is the energy difference between the two legs of the ladder. The Hall polarization can be derived in terms of the ground-state energy derivatives [23–25]. In this sense, following the notations of Ref. [25], we expand the ground-state energy $\mathcal{E}_0(\Phi, \chi, E_y)$ to the third order in Φ, χ, E_y around zero

$$\begin{aligned}\mathcal{E}_0(\tilde{\Phi},\chi,E_y) = & \mathcal{E}_0(0,0,0)+\frac{\tilde{\Phi}^2}{2}\frac{\partial^2\mathcal{E}_0}{\partial\tilde{\Phi}^2}+\frac{\chi^2}{2}\frac{\partial^2\mathcal{E}_0}{\partial\chi^2}\\ & +\frac{E_y^2}{2}\frac{\partial^2\mathcal{E}_0}{\partial E_y^2}+\tilde{\Phi}\chi E_y\frac{\partial^3\mathcal{E}_0}{\partial\tilde{\Phi}\partial\chi\partial E_y},\end{aligned} \tag{6}$$

where we considered only the terms that do not vanish owing to symmetries. The current and density imbalance can be computed as derivatives of the energy as

$$\langle J_x\rangle^{\text{eq}} = L\frac{\partial\mathcal{E}_0}{\partial\tilde{\Phi}}, \quad \langle P_y\rangle^{\text{eq}} = \frac{\partial\mathcal{E}_0}{\partial E_y}. \tag{7}$$

Around the expansion point we have

$$\langle \boldsymbol{J}_x \rangle^{\mathrm{eq}} = L\tilde{\Phi}\left.\frac{\partial^2 \mathcal{E}_0}{\partial \tilde{\Phi}^2}\right|_{\chi,\tilde{\phi},E_y=0},$$
$$\langle P_y \rangle^{\mathrm{eq}} = E_y \frac{\partial^2 \mathcal{E}_0}{\partial E_y^2} + \tilde{\Phi}\chi \left.\frac{\partial^3 \mathcal{E}_0}{\partial \tilde{\Phi}\partial\chi\partial E_y}\right|_{\chi,\tilde{\phi},E_y=0}. \quad (8)$$

As we do not require a finite value of E_y to compute the Hall polarization we obtain the following expression for the equilibrium value [25]:

$$P_H^{\mathrm{eq}} = \frac{\chi}{L}\left.\frac{\frac{\partial^3 \mathcal{E}_0}{\partial\tilde{\phi}\partial\chi\partial E_y}}{\frac{\partial^2 \mathcal{E}_0}{\partial\tilde{\phi}^2}}\right|_{\chi,\tilde{\phi},E_y=0}. \quad (9)$$

A. Noninteracting limit

In the noninteracting limit, $U = 0$, for the Hamiltonian in Eq. (5) we can compute the dispersion relation of the bosonic atoms

$$E_{\pm}(k) = -2J_{\parallel}\cos(k+\tilde{\Phi}/L)\cos(\chi) \pm \{2J^2[1+\cos(k+\tilde{\Phi}/L)] + [E_y + 2J_{\parallel}\sin(k+\tilde{\Phi}/L)\sin(\chi)]^2\}^{1/2}. \quad (10)$$

At small values of the flux χ, where Eq. (9) is valid, we are in the Meissner phase and the minimum of the lower band of the dispersion is at momentum $k = 0$ [41]. Thus, using $\mathcal{E}_0 = E_-(k=0)$ in Eq. (9) we obtain

$$P_H^{\mathrm{eq},U=0} = \frac{-2(J_{\parallel}/J)\chi\cos(\chi)}{1+4(J_{\parallel}/J)\cos(\chi)-4(J_{\parallel}/J)^2\sin(\chi)^2}. \quad (11)$$

We note that even though this relation is derived only for small χ, we kept in the ground-state energy the full dependence on the flux χ. We compare this expression with numerical results at small interaction strengths in Sec. VI B and we find a very good agreement.

B. Mean-field approach in the Meissner phase

In the limit of large atomic fillings ρ in the Meissner phase we can approximate the bosonic operator $b_{j,m} = \sqrt{\rho + \frac{1}{2}(-1)^m\delta\rho}\, e^{i\phi}$. The values of $\delta\rho$ and ϕ can be computed from the minimization of the energy. Furthermore, from the approximate value of the ground-state energy we can obtain the Hall polarization [25]. In this mean-field approximation the Hamiltonian $\tilde{H}$, Eq. (5), for $E_y = 0$ reads

$$\tilde{H} = -2J_{\parallel}L\left[\cos(\chi+\tilde{\Phi}/L)\left(\rho-\frac{1}{2}\delta\rho\right) + \cos(\chi+\tilde{\Phi}/L)\left(\rho+\frac{1}{2}\delta\rho\right)\right] - 4JL\cos(\tilde{\Phi}/2L)\left(\rho^2-\frac{\delta\rho^2}{4}\right)^{1/2} + UL\left(\rho^2-\rho+\frac{\delta\rho^2}{4}\right). \quad (12)$$

The energy is minimized for a local atomic imbalance of

$$\delta\rho = \frac{4J_{\parallel}\rho\sin(\chi)\sin(\tilde{\Phi}/L)}{2J\cos(\tilde{\Phi}/L)+\rho U}. \quad (13)$$

By computing the total current as the derivative of the ground-state energy, Eq. (7), and using that $\langle P_y\rangle^{\mathrm{eq}} = L\delta\rho$, we obtain the following mean-field value of the equilibrium Hall polarization:

$$P_H^{\mathrm{eq,MF}} = \frac{-2(J_{\parallel}/J)\sin(\chi)}{1+\frac{\rho U}{2J}+4\frac{J_{\parallel}}{J}\cos(\chi)\left(1+\frac{\rho U}{2J}\right)-4\frac{J_{\parallel}^2}{J^2}\sin(\chi)^2}. \quad (14)$$

We notice that in the limit of $\chi \to 0$ and $\rho \to 0$ it agrees with the noninteracting result $P_H^{\mathrm{eq},U=0}$, Eq. (11).

VI. RESULTS

In the following, we present the results for the Hall polarization throughout the phase diagram of the Hamiltonian, Eq. (1). We initially focus on the filling $\rho = 0.25$, considering the dependence of $\langle\langle P_H\rangle\rangle$ as a function of both the flux χ and the tunneling amplitude $J_{\parallel}/J$ for different values of the on-site interaction U/J. For this value of the filling, we obtain the same quantum phases in the ground state of the model for all values of the interaction considered, as discussed in Sec. VI A for $U/J = 1$ and $U/J = 10$. This allows us to study the dependence of the Hall response within the same phase as a function of U/J.

In the rest of the Results section, we present the behavior of the Hall response throughout the phase diagram, considering the interaction dependence from the weakly to the strongly interacting limits.

A. Overview of the ground-state phase diagram

For a filling of $\rho = 0.25$ in the phase diagram, we observe three distinct quantum phases [41], as shown in Fig. 2. At small values of the flux χ, or small values of the tunneling $J_{\parallel}/J$, we have the *Meissner superfluid* (M-SF). The Meissner superfluid is characterized by vanishing values of currents on the rungs and by chiral currents on the legs of the ladder, and the presence of a single gapless mode. For larger values of the flux χ, a phase that breaks the $\mathbb{Z}_2$ symmetry of the ladder is present, namely the *biased-chiral superfluid* (BC-SF), which is characterized by a finite density imbalance and a single gapless mode. The ground-state manifold is spanned by two states exhibiting finite values of density imbalance between the two legs of opposite signs. Increasing $J_{\parallel}/J$ we enter the *vortex superfluid* (V-SF), characterized by finite values of the currents both on the legs and the rungs of the ladder, and two gapless modes. The current pattern determines a vortex density incommensurate with the ladder geometry, scaling linearly with the flux $\rho_v = \chi/\pi$. Furthermore, at large values of the interaction strength, for certain values of the flux additional vortex periodicities arise, determined by the following relation between the atomic filling and vortex density $\rho_v = 1-\rho$ [28,41]. In Sec. VI E, we further discuss the presence of commensurability effects at large values of the interaction strength.

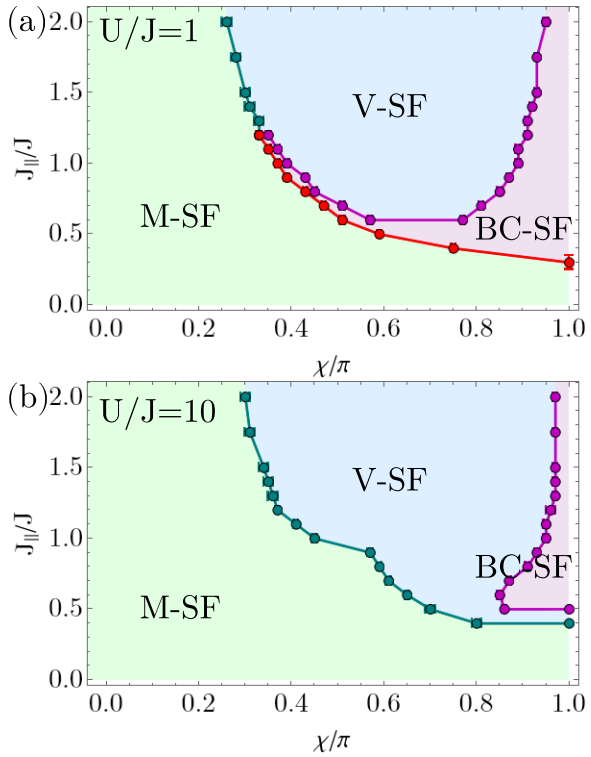

FIG. 2. Sketch of the phase diagram for $\rho = 0.25$ with (a) $U/J = 1$ and (b) $U/J = 10$. The phases present for these parameters are the Meissner superfluid (M-SF), the vortex superfluid (V-SF), and the biased chiral superfluid (BC-SF). The nature of the quantum phases was identified based on DMRG numerical simulations analyzed similarly as in Ref. [41] for a system size of $L = 120$ sites on each leg. The symbols depicted correspond to the values of the flux χ/π at which the phase transitions occur, determined numerically for a fixed value of $J_\parallel/J$. The main characteristics of the phases are described in Sec. VI A.

By increasing the interaction strength from $U/J = 1$ in Fig. 2(a) to $U/J = 10$ in Fig. 2(b), we see that the main changes occurring to the phase boundaries are owing to the sensitivity of the biased-chiral superfluid phase to interactions. For $U/J = 1$, the BC-SF extends to smaller values of the flux, $\chi < 0.5\pi$, and we can trace it as a narrow intermediate phase between the M-SF and V-SF up to at least $J_\parallel/J \approx 1.3$. However, when the interactions increase to $U/J = 10$, the BC-SF only occurs for $\chi \gtrsim 0.85\pi$, and we do not find a direct transition from the M-SF to the BC-SF, but only via the V-SF.

In Fig. 3, we show the behavior of the ground-state observables employed to determine the phase boundaries shown in Fig. 2. We computed the ground-state value of the density imbalance P_y, Eq. (3) [see Fig. 3(a)], which identifies the BC-SF phase, as well as the values of the average rung J_r and chiral currents J_c, defined as

$$J_c = \frac{1}{2(L-1)} \sum_j \langle j^\parallel_{j,1} - j^\parallel_{j,2} \rangle, \quad \text{with}$$
$$j^\parallel_{j,m} = -iJ_\parallel [e^{i\chi(-1)^m} b^\dagger_{j,m} b_{j+1,m} - \text{H.c.}]. \tag{15}$$

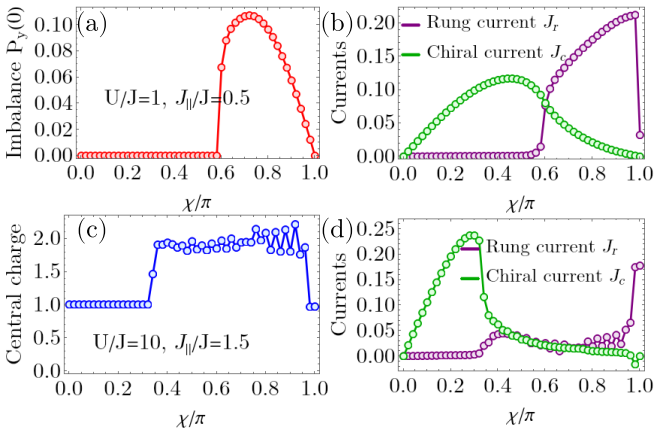

FIG. 3. Ground-state observables employed for the determination of the phase diagram shown in Fig. 2, corresponding to the Hamiltonian given in Eq. (1), for (a)(b) $U/J = 1$ and $J_\parallel/J = 0.5$, and (c)(d) $U/J = 10$ and $J_\parallel/J = 1.5$. We plot in (a) the ground-state value of the density imbalance P_y, Eq. (3), in (b) and (d) the average rung current J_r and the chiral current J_c, defined in Eqs. (15) and (16), and in (c) the central charge, Eq. (17). For the ground-state simulations, we considered a system of $L = 120$ sites on each leg and a bond dimension $m = 750$. Based on the behavior of the observables, we identified for $U/J = 1$ and $J_\parallel/J = 0.5$ a phase transition between M-SF and BC-SF at $\chi \approx 0.59\pi$, and $U/J = 10$ and $J_\parallel/J = 1.5$ a phase transition between M-SF and V-SF at $\chi \approx 0.34\pi$ and between V-SF and BC-SF at $\chi \approx 0.97\pi$.

$$J_r = \frac{1}{2L-1} \sum_j |\langle j^\perp_j \rangle|, \quad \text{with}$$
$$j^\perp_{2j-1} = -iJ(b^\dagger_{j,1} b_{j,2} - \text{H.c.}),$$
$$j^\perp_{2j} = -iJ(b^\dagger_{j+1,1} b_{j,2} - \text{H.c.}). \tag{16}$$

The behavior of the currents [see Figs. 3(b) and 3(d)] can be used to distinguish the Meissner and vortex phases. Furthermore, we determine the number of gapless modes by calculating the central charge c [see Fig. 3(c)], extracted from the scaling of the von Neumann entanglement entropy $S_{vN}(l)$ of a subsystem of length l embedded in the chain of length L. The entanglement entropy for the ground state of gapless phases with open boundary conditions is [55–57]

$$S_{vN} = \frac{c}{6} \log\left(\frac{L}{\pi} \sin \frac{\pi l}{L}\right) + s_1, \tag{17}$$

where s_1 is a nonuniversal constant.

B. The Hall response of the Meissner phase

We begin by analyzing the behavior of the Hall polarization in the Meissner superfluid phase. In Fig. 4, we show the dependence of the steady value of the Hall polarization $\langle\langle P_H \rangle\rangle$ as a function of the flux for small values of $J_\parallel/J \leqslant 0.2$ and different values of the interaction, from almost noninteracting atoms $U/J = 0.1$, to the hard-core limit $U/J = \infty$, within the Meissner superfluid phase. For $J_\parallel/J = 0.05$, Fig. 4(a), the dependence on the flux is almost symmetric with a maximum around the value $\chi/\pi = 0.5$. However, we observe that by

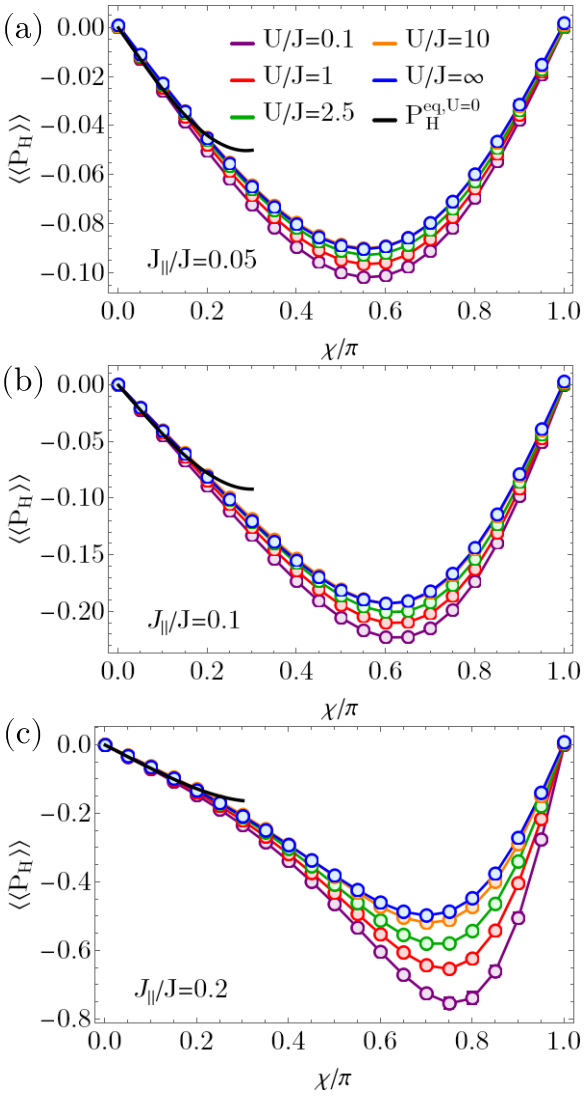

FIG. 4. Time-averaged Hall polarization $\langle\langle P_H\rangle\rangle$ in the Meissner superfluid phase as a function of χ for (a) $J_\parallel/J = 0.05$, (b) $J_\parallel/J = 0.1$, and (c) $J_\parallel/J = 0.2$, for different values of the interaction strength U. The system size is $L = 60$, filling $\rho = 0.25$, and the strength of the linear potential $\mu/J = 0.01$. The black curve at small values of the flux corresponds to the analytical value $P_H^{\mathrm{eq},U=0}$, Eq. (11).

increasing $J_\parallel/J$ the maximum of $\langle\langle P_H\rangle\rangle$ increases in magnitude and moves to higher values of χ. As discussed in Sec. VI C, this is because of the proximity of the phase transitions to the vortex phase or to the biased chiral superfluid, an effect, which is more prominent at lower values of the interaction strength. At low values of the flux, $\chi/\pi \lesssim 0.15$, we have a very good agreement with the equilibrium value of the Hall polarization computed for noninteracting bosons $P_H^{\mathrm{eq},U=0}$. This is also because of the fact that the on-site interaction does not seem to play an important role in this regime, as seen in Fig. 5(a) for $J_\parallel/J = 0.2$ and $\chi/\pi = 0.1$, where for $U/J = 2$ and the hard-core limit, $\langle\langle P_H\rangle\rangle$ is mostly independent of the value of the interaction. However, for larger values of the magnetic flux, e.g., in Fig. 5(b) for $J_\parallel/J = 0.2$ and $\chi/\pi = 0.7$, the value of U/J is much more important, with the magnitude of $\langle\langle P_H\rangle\rangle$ decreasing as the interaction strength increases.

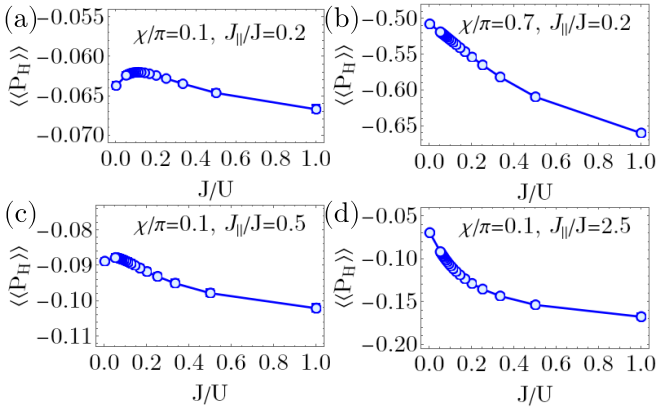

FIG. 5. Time-averaged Hall polarization $\langle\langle P_H\rangle\rangle$ in the Meissner superfluid phase as a function of J/U for (a) $\chi = 0.1\pi$, $J_\parallel/J = 0.2$, (b) $\chi = 0.7\pi$, $J_\parallel/J = 0.2$, (c) $\chi = 0.1\pi$, $J_\parallel/J = 0.5$, and (d) $\chi = 0.1\pi$, $J_\parallel/J = 2.5$. The system size is $L = 90$, filling $\rho = 0.25$, and the strength of the linear potential is $\mu/J = 0.001$.

The good agreement between the analytical expression of $P_H^{\mathrm{eq},U=0}$, Eq. (11), and the numerically determined $\langle\langle P_H\rangle\rangle$ for small values of the interaction, $U/J = 0.1$ and $U/J = 0.2$, can be very well seen in Fig. 6, where we depict $\langle\langle P_H\rangle\rangle$ as a function of $J_\parallel/J$ for small values of χ. The weak dependence on the interaction is confined to small $J_\parallel/J$, while for larger

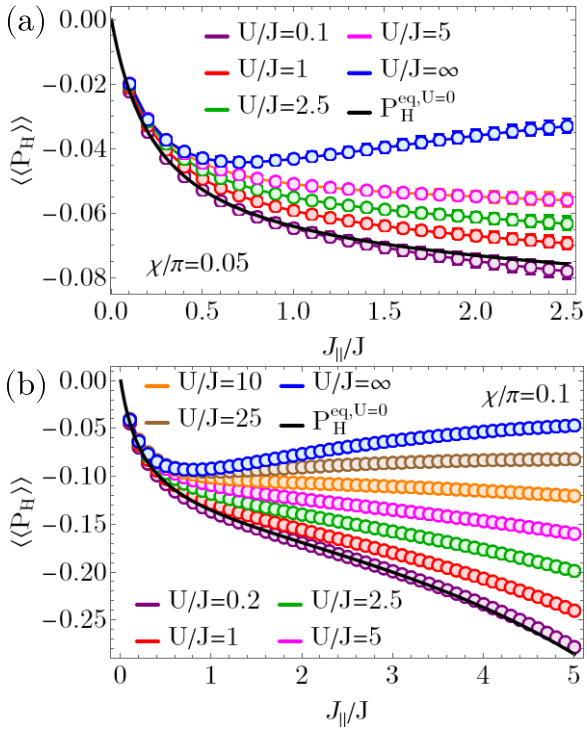

FIG. 6. Time-averaged Hall polarization $\langle\langle P_H\rangle\rangle$ in the Meissner superfluid phase as a function of $J_\parallel/J$ for (a) $\chi = 0.05\pi$, (b) $\chi = 0.1\pi$, for different values of the interaction strength U. The system size is (a) $L = 60$, (b) $L = 90$, filling $\rho = 0.25$ and the strength of the linear potential is (a) $\mu/J = 0.01$, (b) $\mu/J = 0.001$. The black curve at small values of the flux corresponds to the analytical value $P_H^{\mathrm{eq},U=0}$, Eq. (11).

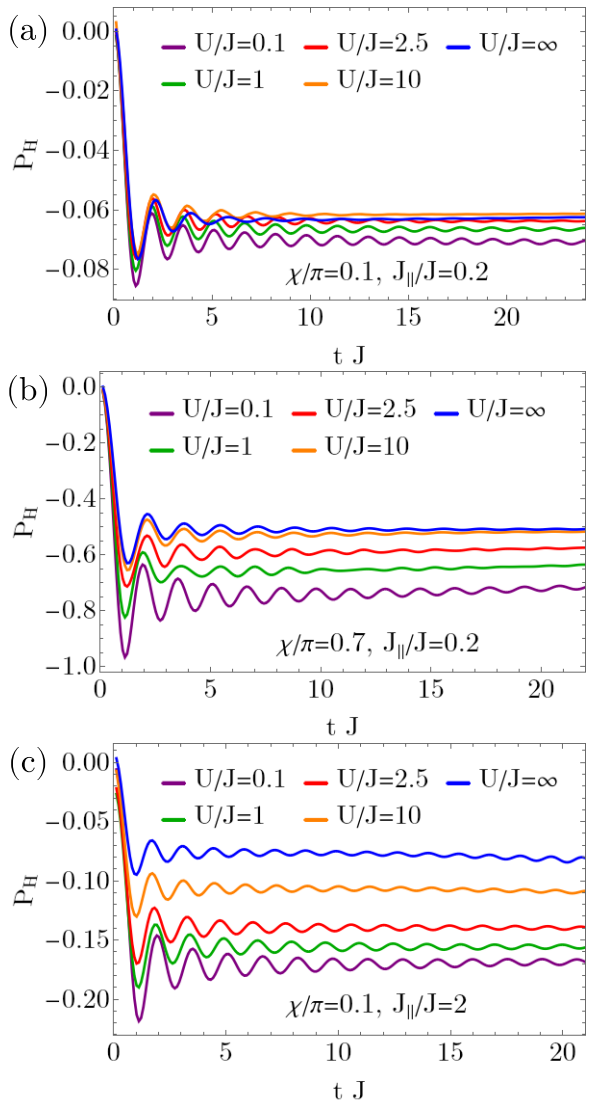

FIG. 7. Time evolution of the Hall polarization $P_H(t)$ in the Meissner superfluid phase for (a) $\chi = 0.1\pi$, $J_\parallel/J = 0.2$, (b) $\chi = 0.7\pi$, $J_\parallel/J = 0.2$, and (c) $\chi = 0.1\pi$, $J_\parallel/J = 2$, for different values of the interaction strength U. The system size is (a)(c) $L = 90$ and (b) $L = 60$, and the strength of the linear potential is (a)(c) $\mu/J = 0.001$ and (b) $\mu/J = 0.01$.

values, we have a much stronger influence of the interaction, as seen in Fig. 5(c) for $J_\parallel/J = 0.5$ compared to Fig. 5(d) for $J_\parallel/J = 2.5$. Furthermore, we observe in Fig. 6 that the value of U/J is crucial for the dependence of $\langle\langle P_H\rangle\rangle$ as a function of $J_\parallel/J$ at larger values of $J_\parallel/J$. While for hard-core bosons the Hall polarization decreases with $J_\parallel/J$, for $U/J \lesssim 10$ $\langle\langle P_H\rangle\rangle$ increases with $J_\parallel/J$ for the interval shown. We associate this with the fact that a phase transition to the vortex superfluid phase may occur for larger values of $J_\parallel/J$ even for the values of χ shown in Fig. 6; e.g., for the noninteracting case, the phase transition occurs for $J_\parallel/J \approx 10$ for $\chi/\pi = 0.1$, see Sec. VI C for more details on the behavior approaching the phase transition.

We depict the dynamics of $P_H(t)$ in the Meissner superfluid phase in Fig. 7 for different values of the interaction strength,

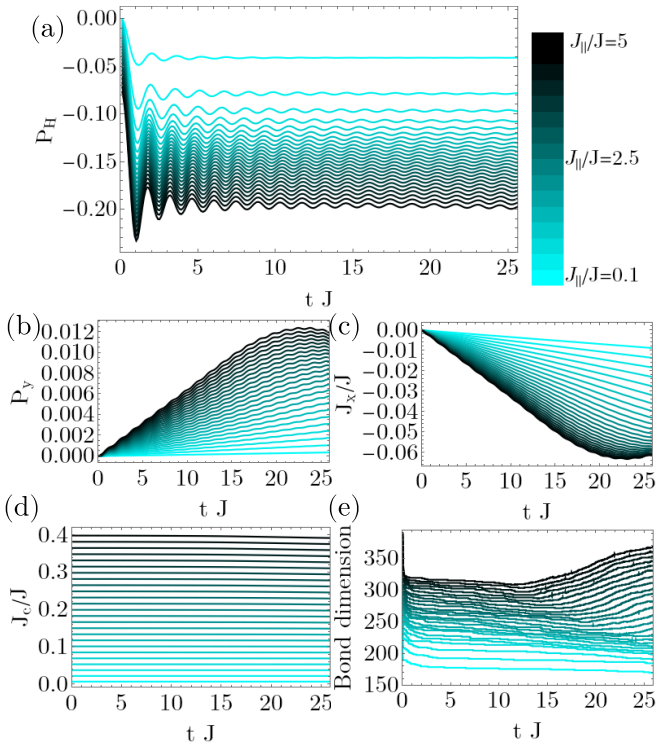

FIG. 8. Time evolution in the Meissner superfluid phase of the (a) Hall polarization P_H, (b) density imbalance P_y, (c) current $\boldsymbol{J}_x/J$, (d) chiral current J_c/J, and (e) bond dimension, for $\chi = 0.1\pi$, $U/J = 2.5$, for different values of the tunneling amplitude $J_\parallel/J$, ranging from $J_\parallel/J = 0.1$ to $J_\parallel/J = 5$. The system size is $L = 90$, and the strength of the linear potential is $\mu/J = 0.001$.

and in Fig. 8(a) varying the strength of $J_\parallel/J$. Throughout the Meissner phase, we observe a similar dynamical behavior, with a fast increase of the magnitude of P_H followed by damped oscillations towards the transient steady value. This steady behavior at long times justifies the study of the time-averaged Hall polarization $\langle\langle P_H\rangle\rangle$. In Fig. 7, we observe, for all parameters depicted, that the oscillations are more prominent for small values of the interaction strength, with the damping increasing with the value of U/J, which also has a slight impact on the frequency of the oscillations.

In Fig. 8, we monitor the state of the system following the quench of the linear potential for $\chi = 0.1\pi$, $U/J = 2.5$ and a wide range of the tunneling $0.1 \leqslant J_\parallel/J \leqslant 5$, for times up to $tJ = 25$. We observe a well-defined plateau in the Hall polarization [Fig. 8(a)] for times considered, with the value of $\langle\langle P_H\rangle\rangle$ increasing with $J_\parallel/J$ for these parameters. Following the quench of the linear potential, the magnitude of both the density imbalance $\langle P_y\rangle$ and the current $\langle \boldsymbol{J}_x\rangle$ exhibit a mostly linear increase. For larger values of $J_\parallel/J$, we see a deviation from the linear trend for times $tJ \gtrsim 20$, stemming from the finite size of the ladder considered here. For larger system sizes, or smaller values of the linear potential μ/J, the deviation from the linear evolution would occur at later times. Interestingly, for the parameters and times considered, we see that the plateau value of P_H is not affected.

In order to analyze the nature of the state during the evolution, we compute the dynamics of the chiral current, defined

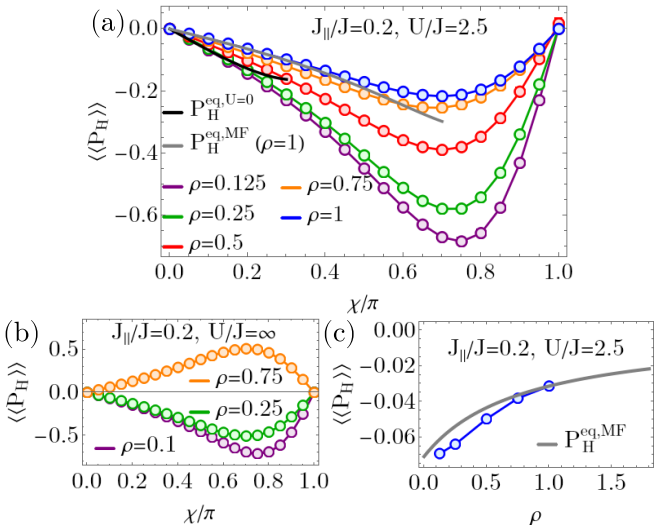

FIG. 9. Time-averaged Hall polarization $\langle\langle P_H\rangle\rangle$ in the Meissner superfluid phase as a function of χ for (a) $J_\parallel/J = 0.2$, $U/J = 2.5$, (b) $J_\parallel/J = 0.2$, $U/J = \infty$, for different values of the filling ρ, and (c) as a function of ρ for $J_\parallel/J = 0.2$, $U/J = 2.5$. The system size is (a)(c) $L = 60$ and (b) $L = 90$, and the strength of the linear potential is (a)(c) $\mu/J = 0.01$ and (b) $\mu/J = 0.001$. The black curve at small values of the flux corresponds to the analytical value $P_H^{\mathrm{eq},U=0}$, Eq. (11), and the gray curve corresponds to the analytical value $P_H^{\mathrm{eq,MF}}(\rho = 1)$, Eq. (14). We note that in (b) the values shown for $\rho = 0.25$, $U/J = \infty$ are taken from Ref. [28].

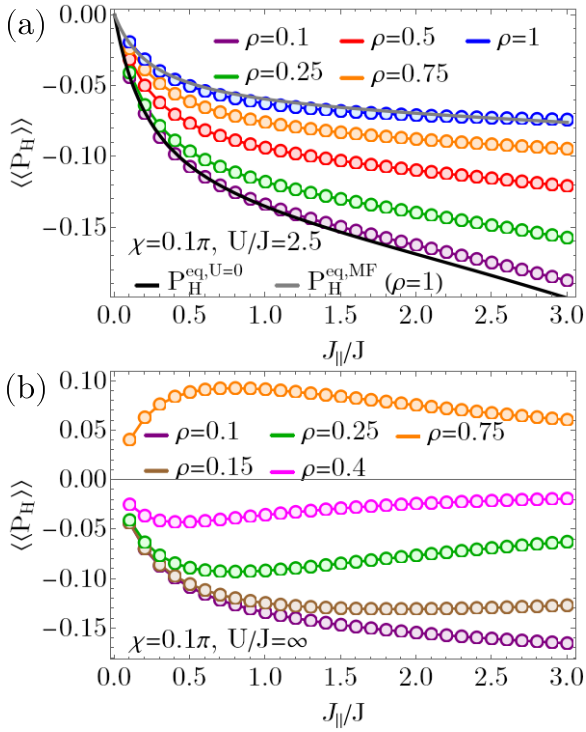

FIG. 10. Time-averaged Hall polarization $\langle\langle P_H\rangle\rangle$ in the Meissner superfluid phase as a function of $J_\parallel/J$ for $\chi = 0.1\pi$ and (a) $U/J = 2.5$, (b) $U/J = \infty$, for different values of the filling ρ. The system size used is $L = 90$, and the strength of the linear potential is $\mu/J = 0.001$. In (a), the black curve at small values of the flux corresponds to the analytical value $P_H^{\mathrm{eq},U=0}$, Eq. (11), and the gray curve corresponds to the analytical value $P_H^{\mathrm{eq,MF}}(\rho = 1)$, Eq. (14).

in Eq. (15). We see that $J_c(t)$ remains constant in time and equal to its ground-state value, Fig. 8(d). This implies that the system maintains its Meissner superfluid character also after the quench during the time interval in which we extract its Hall response. Furthermore, in Fig. 8(e), we show the evolution of the bond dimension used to represent the state of the system as a MPS, which roughly quantifies the amount of entanglement present [49]. We observe that by keeping the truncation error fixed to 10^{-12} the bond dimension decreases abruptly at short times and remains almost constant during the time interval characterized by a linear evolution of P_y and $\boldsymbol{J}_x$. We associate the increase at late times with the growing importance of boundary effects, thus offering a further handle to the estimation of the influence of finite size.

In the final part of the section regarding the Hall response in the Meissner superfluid phase, we analyze the role of the atomic filling ρ with the results presented in Figs. 9 and 10. For a finite interaction strength of $U/J = 2.5$ increasing the atomic filling decreases the magnitude of the Hall polarization, as seen in Fig. 9(a) as a function of χ for $J_\parallel/J = 0.2$ and in Fig. 10(a) as a function of $J_\parallel/J$ for $\chi = 0.1\pi$. In the case of small values of ρ we compare our numerical results with the analytical result $P_H^{\mathrm{eq},U=0}$, Eq. (11), [black curves in Figs. 9(a) and 10(a)], as the noninteracting Hall polarization also corresponds to the single particle limit. We obtain a good agreement with $\langle\langle P_H\rangle\rangle$ for $\rho = 0.125$ for a magnetic flux up to $\chi \lesssim 0.15\pi$ [Fig. 9(a)] and for $\rho = 0.1$ and $\chi = 0.1\pi$ for the dependence on $J_\parallel/J$ [Fig. 10(a)]. The second comparison we perform is for larger values of the atomic filling, where we expect the mean-field approach presented in Sec. V B to hold. For $\rho = 1$, $P_H^{\mathrm{eq,MF}}(\rho = 1)$, Eq. (14), agrees well with the numerical results for $\chi \lesssim 0.4\pi$ and the dependence on $J_\parallel/J$, see gray curves in Figs. 9(a) and 10(a). Furthermore, in Fig. 9(c) we see that the agreement with the mean-field result becomes better as we increase ρ.

As for hard-core bosons a particle-hole symmetry is present in the system for $\rho = 0.5$, it is interesting to investigate the dependence on the filling also in this case. We expect that from small fillings the magnitude of the Hall response will decrease with ρ until it vanishes for $\rho = 0.5$ and changes signs for larger fillings, with the same magnitude and opposite signs for ρ and $1 - \rho$. We observe this behavior in Figs. 9(b) and 10(b), in particular we obtain the same value $|\langle\langle P_H\rangle\rangle|$ for $\rho = 0.25$ and $\rho = 0.75$, but $\langle\langle P_H\rangle\rangle$ has opposite sign for the two values of the filling. The change in sign of the Hall polarization offers us an interesting opportunity when $\rho > 0.5$, as in weak interactions $\langle\langle P_H\rangle\rangle$ is negative in the Meissner phase, while for hard-core bosons $\langle\langle P_H\rangle\rangle$ is positive. This implies that by varying the on-site interaction strength from weakly to strongly interacting regimes we can change the sign of the Hall polarization and have a value of U/J for which the Hall response vanishes. For example, we depict this behavior in Fig. 11 for $\rho = 0.75$ for two sets of parameters in the Meissner superfluid phase. It is an interesting open question if a symmetry emerges at the particular value of U/J for which the Hall response vanishes.

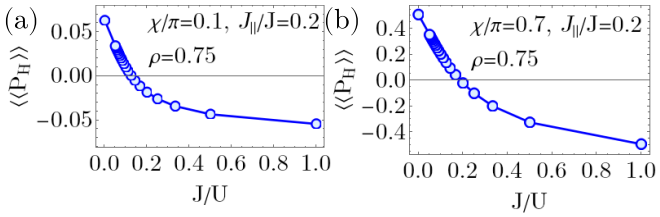

FIG. 11. Time-averaged Hall polarization $\langle\langle P_H\rangle\rangle$ in the Meissner superfluid phase as a function of J/U for (a) $\chi = 0.1\pi$, $J_\parallel/J = 0.2$, (b) $\chi = 0.7\pi$, $J_\parallel/J = 0.2$. The system size is $L = 90$, filling $\rho = 0.75$ and the strength of the linear potential is $\mu/J = 0.001$.

C. Hall response across phase transitions

In the following section, we analyze the behavior of the Hall polarization as we vary the parameters of the model to cross from the Meissner superfluid to the biased-chiral superfluid and the vortex superfluid. In Fig. 12, we show $\langle\langle P_H\rangle\rangle$ as a function of $J_\parallel/J$ for $\chi \in \{0.3\pi, 0.5\pi, 0.8\pi, 0.9\pi\}$ for several values of the interaction, where the system crosses at least one phase boundary. We observe a very rich behavior, with large values of the Hall response, either negative or positive, implying the change of sign of the Hall polarization, and a strong dependence on the value of U/J.

We focus first on the divergence-like feature observed as we approach the phase transition to the vortex or biased phases from the Meissner phase, as we increase $J_\parallel/J$, e.g., around $J_\parallel/J \approx 0.7 - 1.5$ in Fig. 12(a), or around $J_\parallel/J \approx 0.2 - 1.4$ in Fig. 12(c). In Fig. 13, we show $\langle\langle P_H\rangle\rangle$ as a function of $J_\parallel/J$ for $U/J = 1$ for the same values of the flux as in Fig. 12, and the phase transition thresholds are marked with vertical lines. We observe that the large increase of the Hall response in the M-SF corresponds to the presence of a phase transition (also seen in Figs. 14 and 15 as a function of the flux χ). We understand this behavior in the noninteracting limit, as in the following. For $U/J = 0$, the dispersion relation of the Hamiltonian is given by the expression in Eq. (10) for $\tilde{\Phi} = 0$, the lower band exhibits either a single or a double minimum structure depending on the chosen parameters [41]. The Meissner phase is characterized by a single minimum, while the vortex and biased-chiral phase have two minima, with the transition threshold being defined by the parameters for which the lower band has a quartic minimum and satisfy the condition $1 + 4(J_\parallel/J)\cos(\chi) - 4(J_\parallel/J)^2 \sin(\chi)^2 = 0$. However, for the parameters satisfying this condition, the current $\langle \boldsymbol{J}_x\rangle^{\text{eq}}$ vanishes, which implies that $P_H^{\text{eq},U=0}$ diverges as we approach the phase boundary from the Meissner phase, owing to the change in the structure of the dispersion relation. In Fig. 14, we see the good agreement as we approach the divergence of $P_H^{\text{eq},U=0}$ (black curves) as a function of χ, with the numerical result for weak interactions of $U/J = 0.1$ (purple points).

In the numerical results at finite interaction strengths, we do not expect that the current will vanish at the phase transition and result in a divergence. However, for our protocol, in which we quench a linear potential, presented in Sec. II, even if the arising current is nonzero, it can have values comparable to the amplitude of the oscillations present at short times. Thus, for weak interactions close to the phase boundary between M-SF and V-SF, or BC-SF, the short-time oscillations

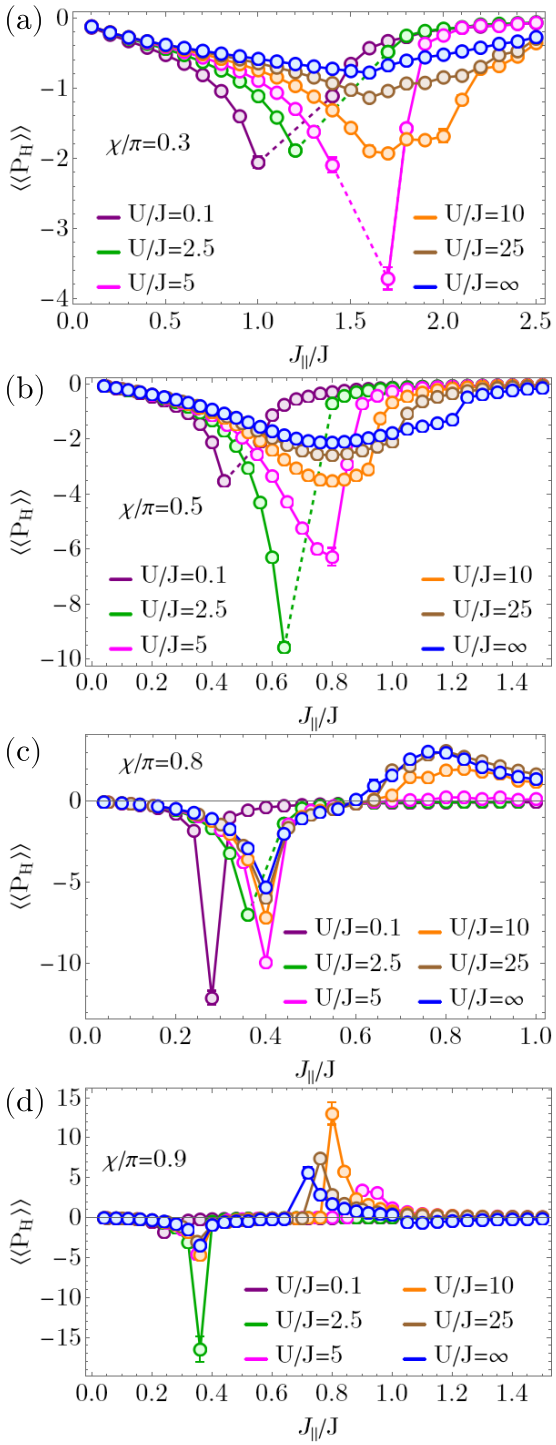

FIG. 12. Time-averaged Hall polarization $\langle\langle P_H\rangle\rangle$ across phase transitions as a function of $J_\parallel/J$ for (a) $\chi = 0.3\pi$, (b) $\chi = 0.5\pi$, (c) $\chi = 0.8\pi$, and (d) $\chi = 0.9\pi$, for different values of the interaction strength U. The system size is $L = 90$, filling $\rho = 0.25$ and the strength of the linear potential is $\mu/J = 0.001$. Dashed lines denote the region where we could not define the value of $\langle\langle P_H\rangle\rangle$ because the current crosses zero during the time evolution.

of current can determine a zero value of the current at certain points in time, which can prevent a well-defined Hall polarization, Eq. (4). For example, in Fig. 16(a) for $U/J = 1$, we have a nicely behaved $P_H(t)$ for $0.8 \leqslant J_\parallel/J \leqslant 1.1$, but for larger

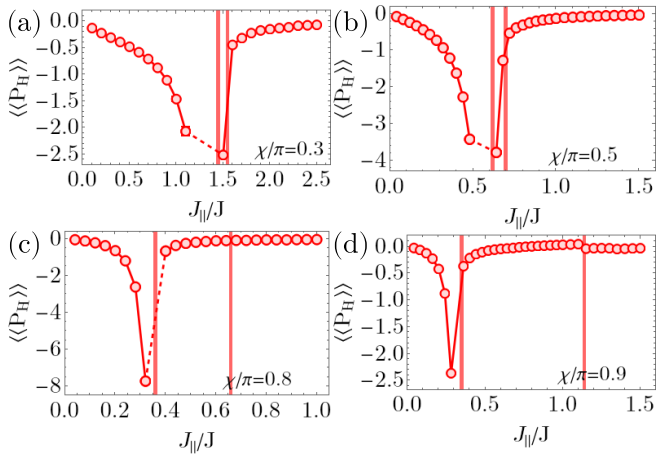

FIG. 13. Time-averaged Hall polarization $\langle\langle P_H\rangle\rangle$ across phase transitions as a function of $J_\parallel/J$ for (a) $\chi = 0.3\pi$, (b) $\chi = 0.5\pi$, (c) $\chi = 0.8\pi$, and (d) $\chi = 0.9\pi$, for $U/J = 1$. The system size is $L = 90$, filling $\rho = 0.25$ and the strength of the linear potential is $\mu/J = 0.001$. The vertical lines denote the phase transition threshold values as marked in the ground-state phase diagrams in Fig. 2. Dashed lines denote the region where we could not define the value of $\langle\langle P_H\rangle\rangle$ because the current crosses zero during the time evolution.

values of the tunneling, $1.2 \leqslant J_\parallel/J \leqslant 1.5$, the current crosses zero at several points in time, as seen in Fig. 16(c). This is the reason why in Figs. 12 and 13 for small values of the interactions, $U/J \lesssim 2$, we have points missing for certain values of the tunneling amplitude $J_\parallel/J$, where we could not properly define a time-averaged $\langle\langle P_H\rangle\rangle$ (regions marked by dashed lines). Roughly, for values larger than $U/J = 2.5$, we do not see the current crossing zero in its time evolution for the parameters considered. For $U/J = 10$, results shown in Fig. 17, we observe oscillations in both the current and the density imbalance [Figs. 17(b) and 17(c)], but since the magnitude of the current is large enough, we can extract a meaningful Hall polarization up to the phase boundary. Even if for strong on-site interactions we do not have a divergence of the Hall polarization, we still see an influence of this single particle effect.

Thus, we observe in Figs. 13 and 15 for $U/J = 1$ that, by approaching the phase boundary marking the end of the Meissner phase, $\langle\langle P_H\rangle\rangle$ increases rapidly, with its maximum close to the critical point and, in most cases, followed by an abrupt decrease in its magnitude in the subsequent phase. A strong Hall response is seen for larger values of the interactions (Figs. 12 and 14) close to the phase transition threshold, even in the absence of a divergence. Interestingly, in Fig. 12(b), where the flux is $\chi = 0.5\pi$, for $U/J \geqslant 10$ we observe that the maximum of $\langle\langle P_H\rangle\rangle$ as a function of $J_\parallel/J$ does not correspond to the phase transition threshold, but rather occurs in the Meissner phase. However, even for these parameters, after the phase transition, we see a discontinuous jump in the value of $\langle\langle P_H\rangle\rangle$.

D. The Hall response of the biased-chiral superfluid phase

In this section, we investigate the behavior of the Hall polarization in the biased-chiral superfluid, phase characteristic of the triangular ladder, having its origin in the frustrated

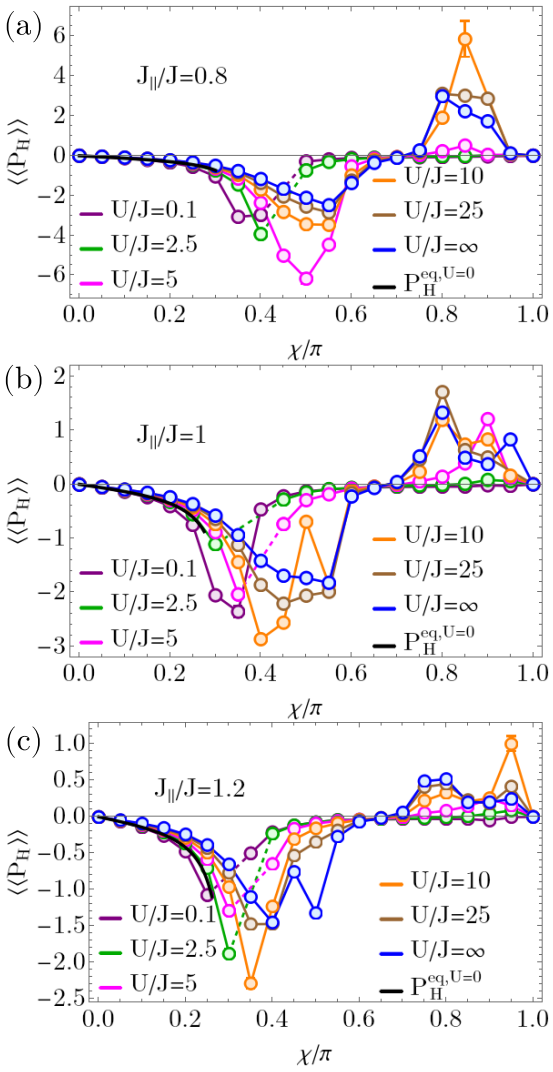

FIG. 14. Time-averaged Hall polarization $\langle\langle P_H\rangle\rangle$ as a function of χ for (a) $J_\parallel/J = 0.8$, (b) $J_\parallel/J = 1$, and (c) $J_\parallel/J = 1.2$, for different values of the interaction strength U. The system size is $L = 90$, filling $\rho = 0.25$ and the strength of the linear potential is $\mu/J = 0.001$. The black curve at small values of the flux corresponds to the analytical value $P_H^{eq,U=0}$, Eq. (11). We note that in (a) the values shown for hard-core bosons, $U/J = \infty$, are taken from Ref. [28]. Dashed lines denote the region where we could not define the value of $\langle\langle P_H\rangle\rangle$ because the current crosses zero during the time evolution.

nature of the system at larger values of the flux [41]. We focus on the parameter regime where the BC-SF phase has a larger extent, e.g., for $\chi = 0.8\pi$ in Fig. 13(c) for $U/J = 1$, we are in the BC-SF for $0.36 \lesssim J_\parallel/J \lesssim 0.66$, or for $\chi = 0.9\pi$ in Fig. 13(d) for $U/J = 1$, we are in the BC-SF for $0.35 \lesssim J_\parallel/J \lesssim 1.14$ and for $U/J = 10$, we are in the BC-SF for $0.46 \lesssim J_\parallel/J \lesssim 0.78$ (see also the phase diagrams in Fig. 2). $\langle\langle P_H\rangle\rangle$ in these regimes has a smooth behavior and relatively small values, in contrast to the behavior close to the transition thresholds, or in the vortex phase (see Sec. VI E). Interestingly, we observe a change of sign of the Hall polarization as we increase the tunneling amplitude $J_\parallel/J$. For this sign change we did not find an explanation similar to the one in Sec. VI B based on the change in the nature of carriers in

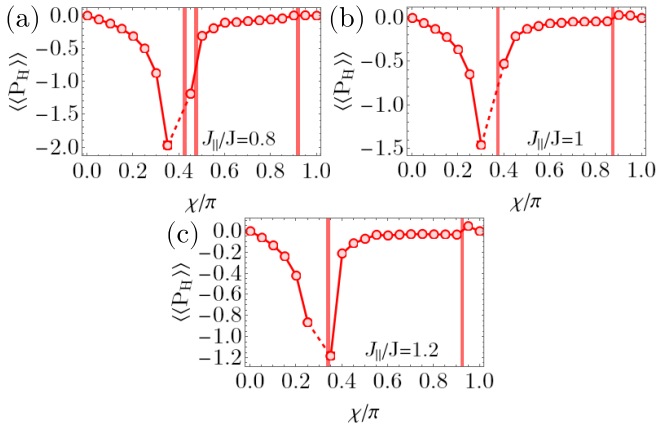

FIG. 15. Time-averaged Hall polarization $\langle\langle P_H\rangle\rangle$ as a function of χ for (a) $J_\parallel/J = 0.8$, (b) $J_\parallel/J = 1$, and (c) $J_\parallel/J = 1.2$, for $U/J = 1$. The system size is $L = 90$, filling $\rho = 0.25$ and the strength of the linear potential $\mu/J = 0.001$. The vertical lines denote the phase transition threshold values marked in the ground-state phase diagrams in Fig. 2. Dashed lines denote the region where we could not define the value of $\langle\langle P_H\rangle\rangle$ because the current crosses zero during the time evolution.

the hard-core regime. At the phase transition between V-SF and BC-SF (marked by the vertical line in Fig. 15 present for $\chi > 0.8\pi$), we observe a small discontinuity in $\langle\langle P_H\rangle\rangle$ as a function of the flux. Furthermore, we obtain the same value of the Hall polarization for both symmetry-broken states that span the ground-state manifold of the BC-SF, regardless of the sign of the ground-state density imbalance.

The dynamics of P_H in the BC-SF is shown in Fig. 18 for $U/J = 1$ and in Fig. 19 for $U/J = 10$, together with the time

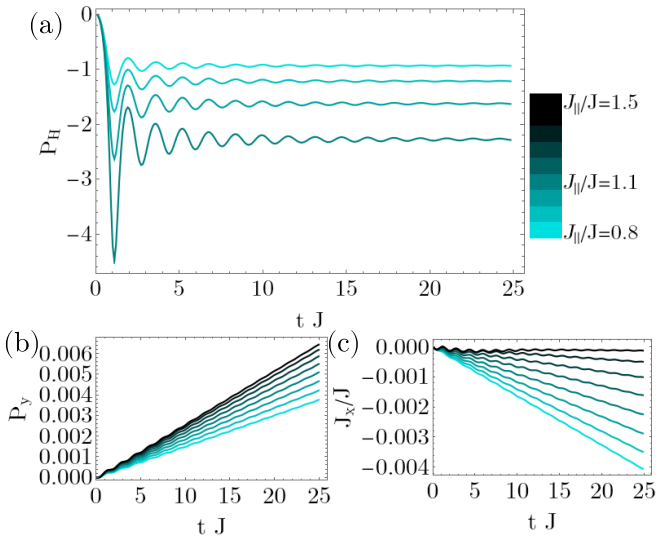

FIG. 16. Time evolution in the Meissner superfluid phase towards the phase transition threshold of the (a) Hall polarization P_H, (b) density imbalance P_y, (c) current $\boldsymbol{J}_x/J$, for $\chi = 0.3\pi$, $U/J = 1$, for different values of the tunneling amplitude $J_\parallel/J$, ranging from $J_\parallel/J = 0.8$ to $J_\parallel/J = 1.1$ for P_H and up to $J_\parallel/J = 1.5$ for P_y and $\boldsymbol{J}_x/J$. The system size is $L = 90$, and the strength of the linear potential is $\mu/J = 0.001$.

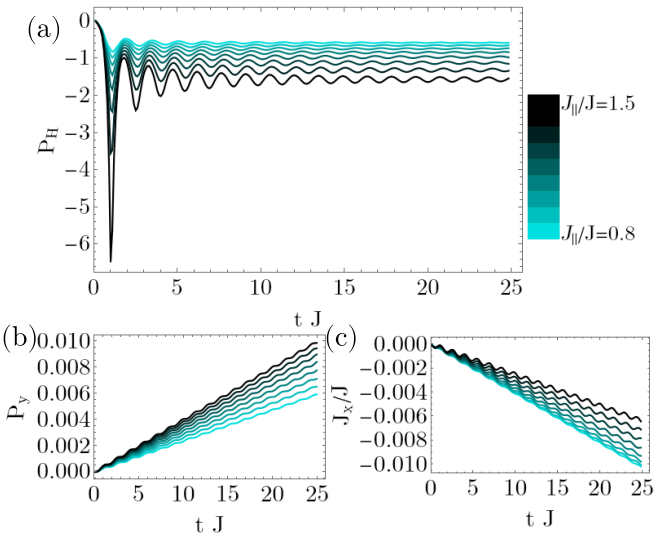

FIG. 17. Time evolution in the Meissner superfluid phase towards the phase transition threshold of the (a) Hall polarization P_H, (b) density imbalance P_y, and (c) current $\boldsymbol{J}_x/J$, for $\chi = 0.3\pi$, $U/J = 10$, for different values of the tunneling amplitude $J_\parallel/J$, ranging from $J_\parallel/J = 0.8$ to $J_\parallel/J = 1.5$. The system size is $L = 90$, and the strength of the linear potential is $\mu/J = 0.001$.

dependence of the density imbalance P_y and current $\boldsymbol{J}_x/J$. We observe that for both weak and strong interactions, the dynamical behavior in the biased phase is different compared to what we saw in the previous section for the Meissner phase, giving further motivation to investigate the dynamics of the Hall polarization and not only its steady value. In the case of $U/J = 1$, Fig. 18(a), close to the phase boundary for $J_\parallel/J = 0.36$, the Hall polarization reaches a steady value only for times $tJ \gtrsim 20$, while for larger values $J_\parallel/J$, deeper in

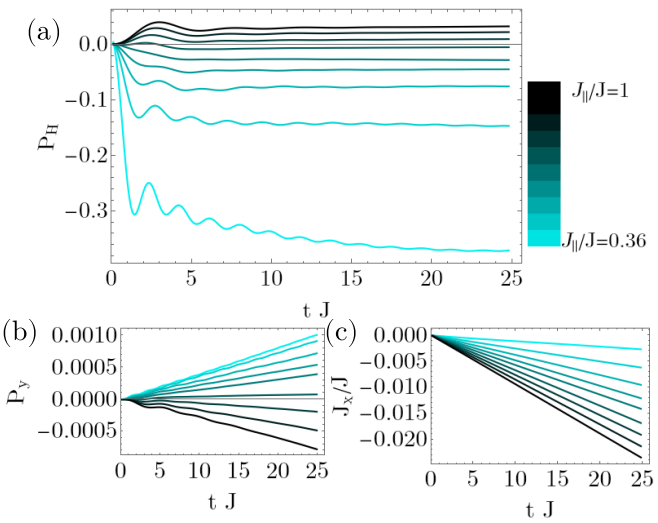

FIG. 18. Time evolution in the biased-chiral superfluid phase of the (a) Hall polarization P_H, (b) density imbalance P_y, (c) current $\boldsymbol{J}_x/J$, for $\chi = 0.9\pi$, $U/J = 1$, for different values of the tunneling amplitude $J_\parallel/J$, ranging from $J_\parallel/J = 0.36$ to $J_\parallel/J = 1$. The system size is $L = 90$, and the strength of the linear potential is $\mu/J = 0.001$.

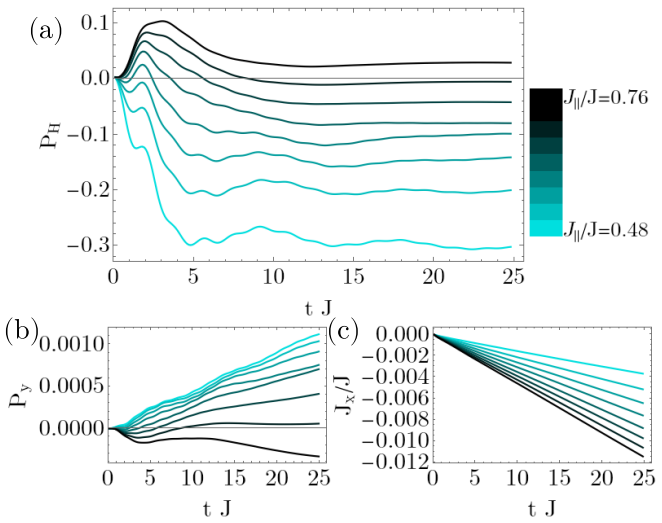

FIG. 19. Time evolution in the biased-chiral superfluid phase of the (a) Hall polarization P_H, (b) density imbalance P_y, (c) current $\boldsymbol{J}_x/J$, for $\chi = 0.9\pi$, $U/J = 10$, for different values of the tunneling amplitude $J_\parallel/J$, ranging from $J_\parallel/J = 0.48$ to $J_\parallel/J = 0.76$. The system size is $L = 90$, and the strength of the linear potential is $\mu/J = 0.001$.

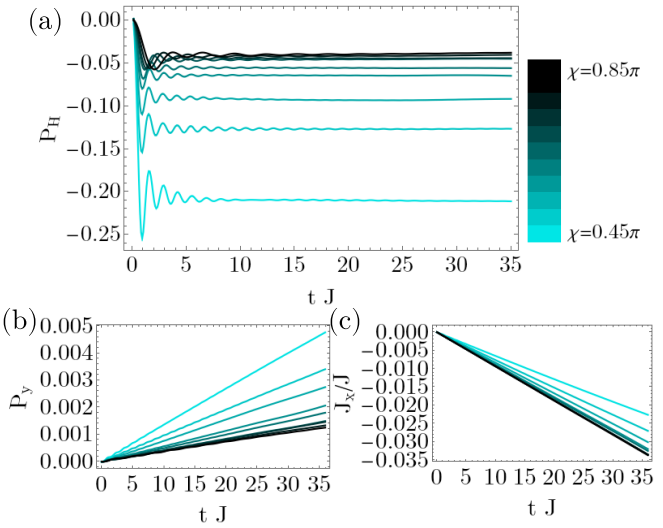

FIG. 20. Time evolution in the vortex superfluid phase of the (a) Hall polarization P_H, (b) density imbalance P_y, (c) current $\boldsymbol{J}_x/J$, for $J_\parallel/J = 1$, $U/J = 1$, for different values of the flux χ, ranging from $\chi = 0.45\pi$ to $\chi = 0.85\pi$. The system size is $L = 90$, and the strength of the linear potential is $\mu/J = 0.001$.

the BC-SF, we reach the transient steady value faster. Near the parameters where $\langle\langle P_H \rangle\rangle$ changes sign, the fast initial oscillations are replaced with a slower oscillatory behavior. The main features of the dynamics, and the change of sign, are caused by the time dependence of the density imbalance P_y, as seen in Fig. 18(b), while the current has a mostly linear time evolution, Fig. 18(c). Similarly, for stronger interactions, $U/J = 10$, shown in Fig. 19, it seems that the oscillatory features of $P_H(t)$ stem from the dynamics of P_y. In this regime, we observe that the sign of P_H is not necessarily determined at short times, as we can have an initial increase to positive values, after which a relaxation to either positive ($J_\parallel/J = 0.76$) or negative ($J_\parallel/J \lesssim 0.72$) values occurs, see Fig. 19(a).

E. Emergence of commensurability effects at large interaction

In this section, we analyze the Hall polarization in the vortex superfluid phase, with a particular focus on commensurability effects, which cause the strong positive response observed in Figs. 12 and 14. We focus on understanding on how the strong positive Hall response emerges as we increase the strength of the interactions. For example, in Figs. 14(a) and 15(a) for $J_\parallel/J = 1$, we observe that for weak interactions in the vortex superfluid phase ($0.37\pi \lesssim \chi \lesssim 0.87\pi$ for $U/J = 1$), the stationary value of the Hall polarization has a smooth behavior with a rather small magnitudes as a function of the flux. In the case of $U/J = 1$, the values remain of $\langle\langle P_H \rangle\rangle$ remain negative, but by increasing the interactions to $U/J = 2.5$, the magnitude of $\langle\langle P_H \rangle\rangle$ is still relatively small, but it exhibits a change of sign. Increasing the interactions to even larger values, we observe a large positive response developing, with a peak around $\chi \approx 0.8\pi$ for $U/J \gtrsim 10$. We can also see this behavior in the time dependence of the Hall polarization, by contrasting the results for $U/J = 1$ shown in Fig. 20 with the ones for $U/J = 10$ shown in Fig. 21. In Fig. 20(a), the dynamics of P_H resembles that in the Meissner phase, e.g., Fig. 8(a), with oscillations at short times that are damped to steady values, even though for $\chi \gtrsim 0.7\pi$, as we approach the transition to the BC-SF, the period of the oscillations is larger and they persist to longer times. This dynamical behavior is in contrast to what we observe in Fig. 21(a) for large values of the on-site interactions. Here, after the sign change of the late time value around $\chi \approx 0.7\pi$, the dynamics is quite different. At very short times, P_H is negative, but afterwards, P_H starts increasing and becomes positive, owing to a sign change of

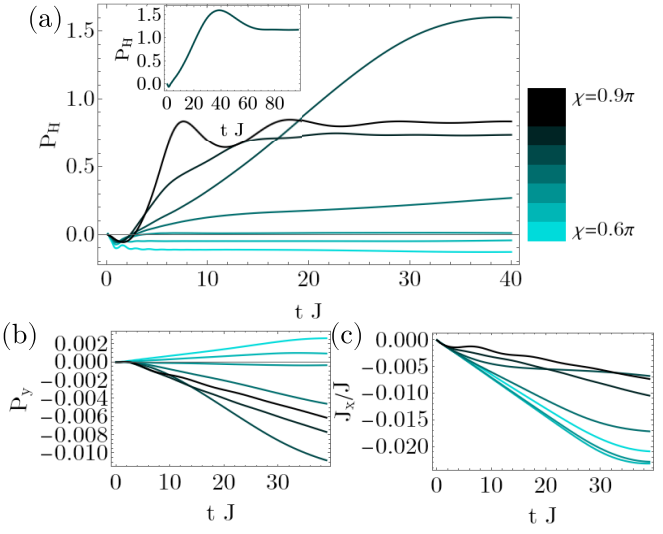

FIG. 21. Time evolution in the vortex superfluid phase of the (a) Hall polarization P_H, (b) density imbalance P_y, (c) current $\boldsymbol{J}_x/J$, for $J_\parallel/J = 1$, $U/J = 10$, for different values of the flux χ, ranging from $\chi = 0.6\pi$ to $\chi = 0.9\pi$. The inset in (a) shows the dynamics of P_H for $\chi = 0.8\pi$ up to longer times. The system size is $L = 90$, and the strength of the linear potential is $\mu/J = 0.001$.

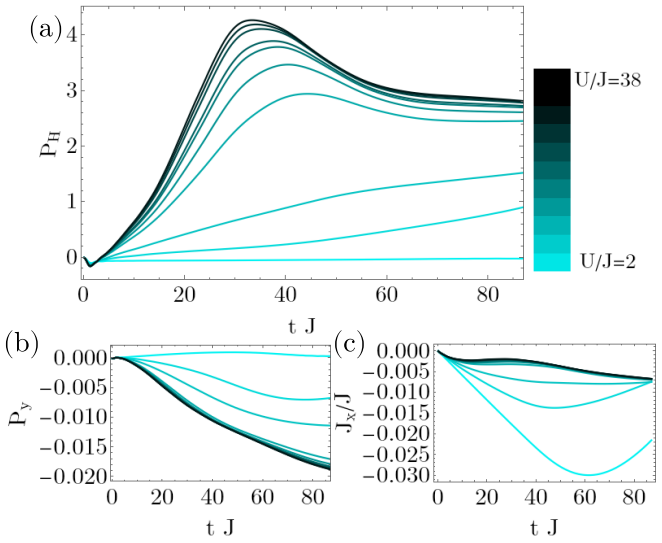

FIG. 22. Time evolution in the vortex superfluid phase of the (a) Hall polarization P_H, (b) density imbalance P_y, and (c) current $\boldsymbol{J}_x/J$, for $J_\parallel/J = 0.76$, $\chi = 0.8\pi$, for different values of the interaction strength U, ranging from $U/J = 2$ to $U/J = 38$. The system size is $L = 90$, and the strength of the linear potential is $\mu/J = 0.001$.

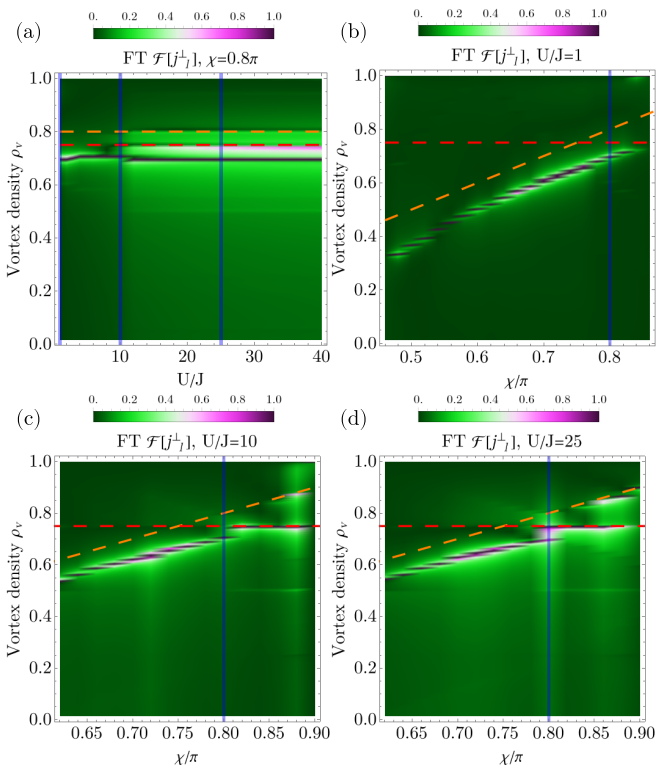

FIG. 23. The Fourier transform of the ground-state local rung currents $j^\perp_j$ as a function of (a) the on-site interactions U/J, (b)–(d) the flux χ for $J_\parallel/J = 0.76$, $\rho = 0.25$ and (a) $\chi = 0.8\pi$, (b) $U/J = 1$, (c) $U/J = 10$, (d) $U/J = 25$. The vertical axis has been scaled in terms of the vortex density ρ_v. The orange-dashed lines correspond to the expectation of the vortex superfluid phase of $\rho_v = \chi/\pi$, the red-dashed lines corresponds to the value $\rho_v = 1 - \rho = 0.75$. The vertical-blue lines mark in (a) the interactions strengths used in (b)–(d), and in (b)–(d) the values of the flux used in (a). The system size is (a) $L = 90$, (b)–(d) $L = 120$. We normalize the Fourier transform such that its maximum is equal to one for each column.

the polarization P_y for these values of the flux, Fig. 21(b). At even longer times, we see a much slower dynamics towards a steady value compared to the other phases investigated so far. In particular, for the largest value of $\langle\langle P_H \rangle\rangle$ occurring at $\chi = 0.8\pi$, a stationary behavior can be identified only for times larger than $tJ \gtrsim 60$ [see inset of Fig. 21(a)].

In Ref. [28], we identified a similar behavior of saturation to large positive values after a slow dynamics in the case of hard-core bosons, which we attributed to the presence of a vortex density commensurately fixed to the value of the atomic filling. We found that the peak of the positive response strongly correlates with the parameters for which the commensurate vortex density dominates the expected incommensurate value of V-SF, for a wide range of parameters and atomic fillings. As this is similar to what we observe at strong finite interaction values, i.e., the strong positive Hall response appears as we increase the on-site interactions alongside the commensurate vortex density, we briefly sketch the origin of the second vortex density value [28]. One approach to deal with the Hamiltonian given in Eq. (1) for the case of hard-core, $U \to \infty$, interactions is to employ a Jordan-Wigner transformation to fermionic operators c_j, $b_j = \prod_{l=1}^{j-1} e^{i\pi c_l^\dagger c_l} c_j$. For a chain geometry, without other interactions, this transformation maps the hard-core bosons to free fermions. In contrast, for our triangular geometry, we obtain an interacting fermionic model as the Jordan-Wigner string does not cancel, and we have in the Hamiltonian a term with four fermionic operators. In Ref. [28] we showed that by varying this term, we interpolate between a free fermions equivalent of Eq. (1) and the hard-core bosons model, and for intermediate values of the fermionic interaction, we obtain a vortex lattice superfluid with the vortex density $\rho_v = 1 - \rho$ determined by the atomic filling. Interestingly, even if we have a phase transition to the incommensurate vortex superfluid as we approach the hard-core bosons model, we can still identify a peak corresponding to $\rho_v = 1 - \rho$ in the Fourier transform of the rung currents, which correlates with a large positive value of the Hall polarization.

In Fig. 22(a), we show the time dependence of P_H for a wide range of the interactions, $2 \leqslant U/J \leqslant 38$ up to long times, $tJ \gtrsim 80$, for parameters where in the strongly interacting limit, we observe a strong positive response, for $J_\parallel/J = 0.76$ and $\chi = 0.8\pi$. For $U/J = 2$, we obtain a small negative stationary value; however, we can only follow the dynamics up to times $tJ \approx 50$ before the finite-size effects become important, as seen in the change of the monotony of the current in Fig. 22(c). Similarly, for the next two interaction strength values, $U/J = 6$ and $U/J = 10$, the finite-size effects become relevant before we can identify a stationary Hall polarization. However, at even larger values, $U/J > 10$, we can reliably compute the Hall polarization up to long times of $tJ \approx 80$ and identify a plateau for $tJ \gtrsim 60$ where P_H stabilizes after a slow increase and an intermediate maximum. Next, we correlate the behavior of the Hall polarization with the ground-state vortex density. We define the vortex density of the V-SF as the values where we have a well-defined peak in the Fourier

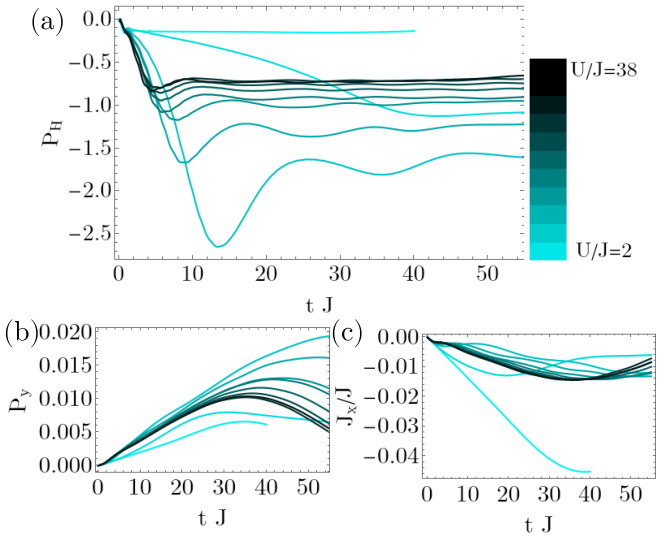

FIG. 24. Time evolution in the vortex superfluid phase of the (a) Hall polarization P_H, (b) density imbalance P_y, and (c) current J_x/J, for $J_\parallel/J = 2$, $\chi = 0.3\pi$, for different values of the interaction strength U, ranging from $U/J = 2$ to $U/J = 38$. The system size is $L = 90$, and the strength of the linear potential is $\mu/J = 0.001$.

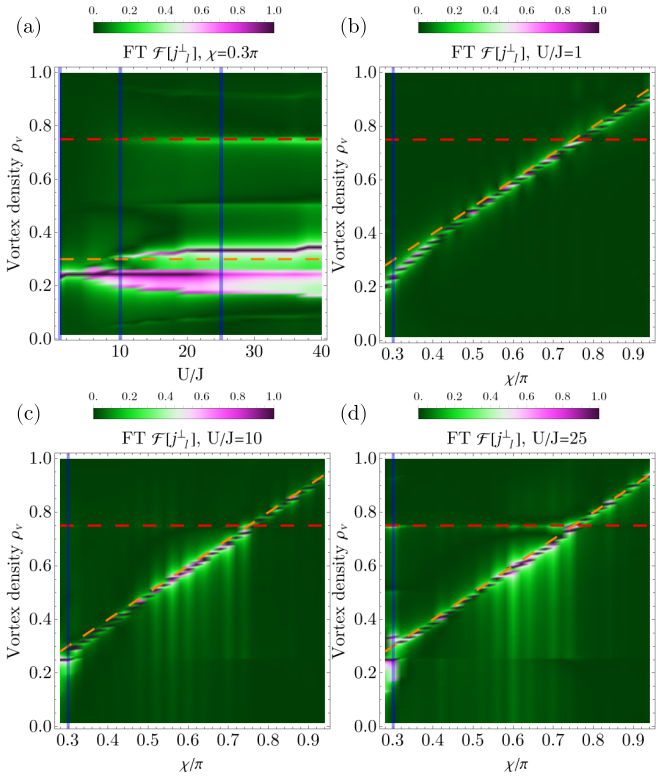

FIG. 25. The Fourier transform of the ground-state local rung currents, $j^\perp_j$, as a function of (a) the on-site interactions U/J, (b)–(d) the flux χ for $J_\parallel/J = 2$, $\rho = 0.25$ and (a) $\chi = 0.3\pi$, (b) $U/J = 1$, (c) $U/J = 10$, (d) $U/J = 25$. The vertical axis has been scaled in terms of the vortex density ρ_v. The orange -dashed lines correspond to the expectation of the vortex superfluid phase of $\rho_v = \chi/\pi$, and the red-dashed lines correspond to the value $\rho_v = 1 - \rho = 0.75$. The vertical-blue lines mark in (a) the interactions strengths in (b)–(d), and in (b)–(d) the values of the flux used in (a). The system size is (a) $L = 90$, (b)–(d) $L = 120$. We normalize the Fourier transform such that its maximum is equal to one for each column.

transform of the ground-state local rung currents, as shown in Fig. 23. In Fig. 23(a), we show the Fourier transform of the rung currents as a function of U/J. We see that for weak interaction, we have a single vortex density, $\rho_v \approx 0.7$, while around $U/J \approx 10$, multiple peaks appear in the Fourier transform, leading to the identification of multiple vortex densities. This corresponds exactly to the parameter regime of the large positive values of the Hall polarization. To better understand the vortex densities values present in the Fourier transform, we plot the dependence on the flux for different U/J in Figs. 23(b)–23(d). For $U/J = 1$, Fig. 23(b), we have a single vortex density varying linearly with the flux, corresponding to the expected incommensurate value of the vortex superfluid. We note the relation $\rho_v = \chi/\pi$ is only valid for large values of $J_\parallel/J$ [41], but in Fig. 23, we consider $J_\parallel/J = 0.76$, explaining why, even if ρ_v has a linear dependence, it does not exactly agree with the value χ/π. If we increase the interactions to $U/J = 10$ and $U/J = 25$ in Figs. 23(c) and 23(d), we observe an additional peak in the Fourier transform from which we can identify a vortex density, $\rho_v = 0.75 = 1 - \rho$, where the value is related to the atomic filling [28]. In particular, we see that this commensurate vortex density dominates around $0.8\pi \lesssim \chi \lesssim 0.85\pi$, but without changing the two-mode gapless nature of the vortex phase [41]. For these values, the incommensurate vortex density show a behavior similar to an avoided crossing, which explains why in Fig. 23(a) we see three peaks in the Fourier transform at $\chi = 0.8\pi$. We observe the same phenomenology for the other parameters where we see a large positive value of $\langle\langle P_H \rangle\rangle$ [see Figs. 12(c), 12(d), and 14(a)–14(c)], with a similar correspondence to the appearance of a dominant peak in the Fourier transform of the rung currents at $\rho_v = 1 - \rho$.

In the last part of this section, we discuss the behavior of the Hall polarization for $\chi = 0.3\pi$ as we enter the vortex superfluid phase, shown in Fig. 12(a). Compared to our previous discussion (see Sec. VI C), we see an unusual behavior for $U/J = 10$ where $\langle\langle P_H \rangle\rangle$ does not exhibit a drop in its magnitude after crossing the phase boundary at $J_\parallel/J \approx 1.65$, as observed for the other parameters. One explanation for this could be that for $U/J = 10$ and $\chi = 0.3\pi$ by plotting $\langle\langle P_H \rangle\rangle$ as a function of $J_\parallel/J$, we are very close to the phase boundary for $J_\parallel/J \gtrsim 1.65$ [see Fig. 2(b)], while for the other interaction values, the transition threshold is a slightly lower values of the flux. However, it is still interesting to analyze the time dependence of P_H, Fig. 24, and the behavior of the ground-state vortex density, Fig. 25, for these parameters to gain additional insight. We observe in Fig. 24(a) that increasing the interaction strength from $U/J = 2$ to $U/J = 6$ results in a drastic increase in the time scale for reaching the stationary value. For even stronger interactions, $U/J \geqslant 10$, the steady plateau is reached earlier, with the minimal value of $\langle\langle P_H \rangle\rangle$ reached for $U/J = 10$. The dynamics in this regime resembles that shown in Fig. 21(a) for $\chi = 0.9\pi$, but with an opposite sign. By analyzing the behavior of the vortex density, we obtain that $U/J = 10$ is also the value for which multiple peaks in the

Fourier transform of the rung currents appear, Fig. 25(a). For weak interactions [$U/J = 1$ in Fig. 25(b)], the vortex density is dominated by the incommensurate response, $\rho_v = \chi/\pi$, with small deviations for smaller values of the flux close to the transition point to the Meissner phase. However, starting from $U/J = 10$, two additional peaks are present in the Fourier transform, corresponding to the vortex densities $\rho_v = 1 - \rho$ and $\rho_v = \rho$, which seem to lead to a strong Hall response. We note that we did not check for multiple parameter sets that the commensurate vortex density of $\rho_v = \rho$ within the vortex superfluid leads to a large negative value of $\langle\langle P_H \rangle\rangle$, as for the parameters considered in this paper, the vortex phase did not extend to low enough values of the flux. This is in contrast with our analysis for the large positive $\langle\langle P_H \rangle\rangle$ being correlated to the presence of $\rho_v = 1 - \rho$ appearing at larger values of χ, which we observed for many parameter sets.

VII. DISCUSSIONS AND CONCLUSIONS

To summarize, we have investigated the behavior of the Hall polarization for a triangular Bose-Hubbard ladder in a magnetic field, focusing on the effects of the on-site interactions from the weakly interacting regime to the hard-core limit. We compute the time evolution of the system following the quench of a linear potential, which induces a current through the system, analyzing both the short-time nonequilibrium dynamics of the Hall polarization and its long-time saturation value. We show that the Hall polarization can be employed to fingerprint and probe many of the features of the underlying ground-state phase diagram, being particularly sensitive to the phase boundaries and the interplay of commensurate-incommensurate effects occurring at strong interactions. In the noninteracting limit, the equilibrium Hall polarization diverges as we approach the phase transition from the M-SF to the V-SF or BC-SF. Interestingly, this single particle effect can still determine a very strong negative Hall response in the regimes of strong interactions. Our results show the possibility of changing the sign of the Hall polarization, for some parameter sets, e.g., large fillings $\rho > 0.5$ and strong interactions. This can be explained by the change in the character of the carriers from particles to holes, while for other regimes, e.g., $\rho = 0.25$ in the V-SF and BC-SF, we do not have a similar argument. Sign changes in the Hall response have previously been linked to the presence of a topological phase transition [58,59]. We can correlate the strong positive values of the Hall polarization present for strong interactions to the presence of a commensurate vortex density in the otherwise incommensurate vortex superfluid.

We expect that our paper will be experimentally relevant in the near future, as the Hall response has been measured for ultracold fermionic atoms confined to square ladders [19]. Triangular flux ladders have been realized in momentum space in Ref. [60], or could be achieved in real space by employing optical lattices at the antimagic wavelength [45]. Further motivation is given by the ongoing experimental interest in exploring frustration-driven quantum phenomena with ultracold atoms in triangular geometries [61–67].

ACKNOWLEDGMENTS

We thank J.-S. Bernier, M. Filippone for fruitful discussions. This work was supported by the Swiss National Science Foundation under Division II Grant No. 200020-219400.

[1] A. Kitaev, Fault-tolerant quantum computation by anyons, Ann. Phys. (NY) **303**, 2 (2003).
[2] C. Nayak, S. H. Simon, A. Stern, M. Freedman, and S. Das Sarma, Non-Abelian anyons and topological quantum computation, Rev. Mod. Phys. **80**, 1083 (2008).
[3] D. C. Tsui, H. L. Stormer, and A. C. Gossard, Two-dimensional magnetotransport in the extreme quantum limit, Phys. Rev. Lett. **48**, 1559 (1982).
[4] R. B. Laughlin, Anomalous quantum Hall effect: An incompressible quantum fluid with fractionally charged excitations, Phys. Rev. Lett. **50**, 1395 (1983).
[5] H. L. Stormer, D. C. Tsui, and A. C. Gossard, The fractional quantum Hall effect, Rev. Mod. Phys. **71**, S298 (1999).
[6] J. Dalibard, F. Gerbier, G. Juzeliūnas, and P. Öhberg, *Colloquium*: Artificial gauge potentials for neutral atoms, Rev. Mod. Phys. **83**, 1523 (2011).
[7] N. Goldman, G. Juzeliūnas, P. Öhberg, and I. B. Spielman, Light-induced gauge fields for ultracold atoms, Rep. Prog. Phys. **77**, 126401 (2014).
[8] P. Hauke and I. Carusotto, Quantum Hall and synthetic magnetic-field effects in ultra-cold atomic systems, *Encyclopedia of Condensed Matter Physics*, 2nd ed., editied by T. Chakraborty (Academic Press, Oxford, 2024), pp. 629–639.
[9] M. Aidelsburger, M. Atala, S. Nascimbène, S. Trotzky, Y.-A. Chen, and I. Bloch, Experimental realization of strong effective magnetic fields in an optical lattice, Phys. Rev. Lett. **107**, 255301 (2011).
[10] J. Struck, C. Ölschläger, M. Weinberg, P. Hauke, J. Simonet, A. Eckardt, M. Lewenstein, K. Sengstock, and P. Windpassinger, Tunable gauge potential for neutral and spinless particles in driven optical lattices, Phys. Rev. Lett. **108**, 225304 (2012).
[11] M. Aidelsburger, M. Atala, M. Lohse, J. T. Barreiro, B. Paredes, and I. Bloch, Realization of the Hofstadter Hamiltonian with ultracold atoms in optical lattices, Phys. Rev. Lett. **111**, 185301 (2013).
[12] H. Miyake, G. A. Siviloglou, C. J. Kennedy, W. C. Burton, and W. Ketterle, Realizing the Harper Hamiltonian with laser-assisted tunneling in optical lattices, Phys. Rev. Lett. **111**, 185302 (2013).
[13] M. Atala, M. Aidelsburger, M. Lohse, J. T. Barreiro, B. Paredes, and I. Bloch, Observation of chiral currents with ultracold atoms in bosonic ladders, Nat. Phys. **10**, 588 (2014).
[14] M. Aidelsburger, M. Lohse, C. Schweizer, M. Atala, J. T. Barreiro, S. Nascimbène, N. R. Cooper, I. Bloch, and N. Goldman, Measuring the Chern number of Hofstadter bands with ultracold bosonic atoms, Nat. Phys. **11**, 162 (2015).
[15] M. Mancini, G. Pagano, G. Cappellini, L. Livi, M. Rider, J. Catani, C. Sias, P. Zoller, M. Inguscio, M. Dalmonte, and L. Fallani, Observation of chiral edge states with neutral

fermions in synthetic Hall ribbons, Science **349**, 1510 (2015).
[16] M. E. Tai, A. Lukin, M. Rispoli, R. Schittko, T. Menke, D. Borgnia, P. M. Preiss, F. Grusdt, A. M. Kaufman, and M. Greiner, Microscopy of the interacting Harper–Hofstadter model in the two-body limit, Nature (London) **546**, 519 (2017).
[17] D. Genkina, L. M. Aycock, H.-I. Lu, M. Lu, A. M. Pineiro, and I. B. Spielman, Imaging topology of Hofstadter ribbons, New J. Phys. **21**, 053021 (2019).
[18] T. Chalopin, T. Satoor, A. Evrard, V. Makhalov, J. Dalibard, R. Lopes, and S. Nascimbene, Probing chiral edge dynamics and bulk topology of a synthetic Hall system, Nat. Phys. **16**, 1017 (2020).
[19] T.-W. Zhou, G. Cappellini, D. Tusi, L. Franchi, J. Parravicini, C. Repellin, S. Greschner, M. Inguscio, T. Giamarchi, M. Filippone, J. Catani, and L. Fallani, Observation of universal Hall response in strongly interacting Fermions, Science **381**, 427 (2023).
[20] J. Léonard, S. Kim, J. Kwan, P. Segura, F. Grusdt, C. Repellin, N. Goldman, and M. Greiner, Realization of a fractional quantum Hall state with ultracold atoms, Nature (London) **619**, 495 (2023).
[21] C. Repellin, J. Léonard, and N. Goldman, Fractional Chern insulators of few bosons in a box: Hall plateaus from center-of-mass drifts and density profiles, Phys. Rev. A **102**, 063316 (2020).
[22] L. Peralta Gavensky, S. Sachdev, and N. Goldman, Connecting the many-body Chern number to Luttinger's theorem through Středa's formula, Phys. Rev. Lett. **131**, 236601 (2023).
[23] P. Prelovšek, M. Long, T. Markež, and X. Zotos, Hall constant of strongly correlated electrons on a ladder, Phys. Rev. Lett. **83**, 2785 (1999).
[24] X. Zotos, F. Naef, M. Long, and P. Prelovšek, Reactive Hall response, Phys. Rev. Lett. **85**, 377 (2000).
[25] S. Greschner, M. Filippone, and T. Giamarchi, Universal Hall response in interacting quantum systems, Phys. Rev. Lett. **122**, 083402 (2019).
[26] M. Buser, S. Greschner, U. Schollwöck, and T. Giamarchi, Probing the Hall voltage in synthetic quantum systems, Phys. Rev. Lett. **126**, 030501 (2021).
[27] R. Citro, T. Giamarchi, and E. Orignac, Hall response in interacting bosonic and fermionic ladders, Phys. Rev. Lett, **134**, 056501 (2025).
[28] C.-M. Halati and T. Giamarchi, Exploring frustration effects of strongly interacting bosons via the Hall response, Phys. Rev. Res. **7**, 013199 (2025).
[29] A. Lopatin, A. Georges, and T. Giamarchi, Hall effect and interchain magneto-optical properties of coupled Luttinger liquids, Phys. Rev. B **63**, 075109 (2001).
[30] G. León, C. Berthod, and T. Giamarchi, Hall effect in strongly correlated low-dimensional systems, Phys. Rev. B **75**, 195123 (2007).
[31] A. Auerbach, Hall number of strongly correlated metals, Phys. Rev. Lett. **121**, 066601 (2018).
[32] M. Filippone, C.-E. Bardyn, S. Greschner, and T. Giamarchi, Vanishing Hall response of charged fermions in a transverse magnetic field, Phys. Rev. Lett. **123**, 086803 (2019).
[33] T. Mishra, R. V. Pai, S. Mukerjee, and A. Paramekanti, Quantum phases and phase transitions of frustrated hard-core bosons on a triangular ladder, Phys. Rev. B **87**, 174504 (2013).
[34] E. Anisimovas, M. Račiūnas, C. Sträter, A. Eckardt, I. B. Spielman, and G. Juzeliūnas, Semisynthetic zigzag optical lattice for ultracold bosons, Phys. Rev. A **94**, 063632 (2016).
[35] F. A. An, E. J. Meier, and B. Gadway, Engineering a flux-dependent mobility edge in disordered zigzag chains, Phys. Rev. X **8**, 031045 (2018).
[36] C. Romen and A. M. Läuchli, Chiral Mott insulators in frustrated Bose-Hubbard models on ladders and two-dimensional lattices: A combined perturbative and density matrix renormalization group study, Phys. Rev. B **98**, 054519 (2018).
[37] S. Greschner and T. Mishra, Interacting bosons in generalized zigzag and railroad-trestle models, Phys. Rev. B **100**, 144405 (2019).
[38] J. Cabedo, J. Claramunt, J. Mompart, V. Ahufinger, and A. Celi, Effective triangular ladders with staggered flux from spin-orbit coupling in 1D optical lattices, Eur. Phys. J. D **74**, 123 (2020).
[39] Y. Li, H. Cai, D.-w. Wang, L. Li, J. Yuan, and W. Li, Many-body chiral edge currents and sliding phases of atomic spin waves in momentum-space lattice, Phys. Rev. Lett. **124**, 140401 (2020).
[40] S. Singha Roy, L. Carl, and P. Hauke, Genuine multipartite entanglement in a one-dimensional Bose-Hubbard model with frustrated hopping, Phys. Rev. B **106**, 195158 (2022).
[41] C.-M. Halati and T. Giamarchi, Bose-Hubbard triangular ladder in an artificial gauge field, Phys. Rev. Res. **5**, 013126 (2023).
[42] L. Barbiero, J. Cabedo, M. Lewenstein, L. Tarruell, and A. Celi, Frustrated magnets without geometrical frustration in bosonic flux ladders, Phys. Rev. Res. **5**, L042008 (2023).
[43] B. Beradze and A. Nersesyan, Spectrum, Lifshitz transitions and orbital current in frustrated fermionic ladders with a uniform flux, Eur. Phys. J. B **96**, 2 (2023).
[44] B. Beradze, M. Tsitsishvili, E. Tirrito, M. Dalmonte, T. Chanda, and A. Nersesyan, Emergence of non-Abelian SU(2) invariance in Abelian frustrated fermionic ladders, Phys. Rev. B **108**, 075146 (2023).
[45] N. Baldelli, C. R. Cabrera, S. Julià-Farré, M. Aidelsburger, and L. Barbiero, Frustrated extended Bose-Hubbard model and deconfined quantum critical points with optical lattices at the antimagic wavelength, Phys. Rev. Lett. **132**, 153401 (2024).
[46] G. León, C. Berthod, T. Giamarchi, and A. J. Millis, Hall effect on the triangular lattice, Phys. Rev. B **78**, 085105 (2008).
[47] S. R. White, Density matrix formulation for quantum renormalization groups, Phys. Rev. Lett. **69**, 2863 (1992).
[48] U. Schollwöck, The density-matrix renormalization group, Rev. Mod. Phys. **77**, 259 (2005).
[49] U. Schollwöck, The density-matrix renormalization group in the age of matrix product states, Ann. Phys. (NY) **326**, 96 (2011).
[50] K. A. Hallberg, New trends in density matrix renormalization, Adv. Phys. **55**, 477 (2006).
[51] E. Jeckelmann, Dynamical density-matrix renormalization-group method, Phys. Rev. B **66**, 045114 (2002).
[52] M. Fishman, S. R. White, and E. M. Stoudenmire, The ITensor software library for tensor network calculations, SciPost Phys. Codebases 4 (2022).
[53] A. J. Daley, C. Kollath, U. Schollwöck, and G. Vidal, Time-dependent density-matrix renormalization-group using adaptive effective Hilbert spaces, J. Stat. Mech. (2004) P04005.
[54] S. R. White and A. E. Feiguin, Real-time evolution using the density matrix renormalization group, Phys. Rev. Lett. **93**, 076401 (2004).

[55] G. Vidal, J. I. Latorre, E. Rico, and A. Kitaev, Entanglement in quantum critical phenomena, Phys. Rev. Lett. **90**, 227902 (2003).

[56] P. Calabrese and J. Cardy, Entanglement entropy and quantum field theory, J. Stat. Mech. (2004) P06002.

[57] C. Holzhey, F. Larsen, and F. Wilczek, Geometric and renormalized entropy in conformal field theory, Nucl. Phys. B **424**, 443 (1994).

[58] S. D. Huber and N. H. Lindner, Topological transitions for lattice bosons in a magnetic field, Proc. Natl. Acad. Sci. USA **108**, 19925 (2011).

[59] E. Berg, S. D. Huber, and N. H. Lindner, Sign reversal of the Hall response in a crystalline superconductor, Phys. Rev. B **91**, 024507 (2015).

[60] Y. Li, H. Du, Y. Wang, J. Liang, L. Xiao, W. Yi, J. Ma, and S. Jia, Observation of frustrated chiral dynamics in an interacting triangular flux ladder, Nat. Commun. **14**, 7560 (2023).

[61] C. Becker, P. Soltan-Panahi, J. Kronjäger, S. Dörscher, K. Bongs, and K. Sengstock, Ultracold quantum gases in triangular optical lattices, New J. Phys. **12**, 065025 (2010).

[62] J. Struck, C. Ölschläger, R. L. Targat, P. Soltan-Panahi, A. Eckardt, M. Lewenstein, P. Windpassinger, and K. Sengstock, Quantum simulation of frustrated classical magnetism in triangular optical lattices, Science **333**, 996 (2011).

[63] J. Yang, L. Liu, J. Mongkolkiattichai, and P. Schauss, Site-resolved imaging of ultracold fermions in a triangular-lattice quantum gas microscope, PRX Quantum **2**, 020344 (2021).

[64] J. Mongkolkiattichai, L. Liu, D. Garwood, J. Yang, and P. Schauss, Quantum gas microscopy of fermionic triangular-lattice Mott insulators, Phys. Rev. A **108**, L061301 (2023).

[65] M. Xu, L. H. Kendrick, A. Kale, Y. Gang, G. Ji, R. T. Scalettar, M. Lebrat, and M. Greiner, Frustration- and doping-induced magnetism in a Fermi–Hubbard simulator, Nature (London) **620**, 971 (2023).

[66] M. Lebrat, M. Xu, L. H. Kendrick, A. Kale, Y. Gang, P. Seetharaman, I. Morera, E. Khatami, E. Demler, and M. Greiner, Observation of Nagaoka polarons in a Fermi–Hubbard quantum simulator, Nature (London) **629**, 317 (2024).

[67] M. L. Prichard, B. M. Spar, I. Morera, E. Demler, Z. Z. Yan, and W. S. Bakr, Directly imaging spin polarons in a kinetically frustrated Hubbard system, Nature (London) **629**, 323 (2024).